Ore Geology Reviews 77 (2016) 246–259

Contents lists available at ScienceDirect

Ore Geology Reviews

journal homepage: www.elsevier.com/locate/oregeorev

Geochemistry of the apulian allochthonous karst bauxite, Southern Italy: Distribution of critical elements and constraints on Late Cretaceous Peri-Tethyan palaeogeography

Giovanni Mongelli [a,*], Roberto Buccione [a], Erwan Gueguen [b], Antonio Langone [c], Rosa Sinisi [a]

[a] Department of Sciences, University of Basilicata, viale dell'Ateneo Lucano 10, 85100 Potenza, Italy
[b] CNR — Istituto di Metodologie per l'Analisi Ambientale, c/da S. Loya, 85050, Tito Scalo, Italy
[c] CNR — Istituto di Geoscienze e Georisorse, via Ferrara 1, 27100 Pavia, Italy

ARTICLE INFO

Article history:
Received 1 September 2015
Received in revised form 29 February 2016
Accepted 1 March 2016
Available online 3 March 2016

Keywords:
Karst bauxite
Critical elements
Concretions growth
Bauxite protolith(s)
Late Cretaceous
Peri-Tethyan domain

ABSTRACT

A comprehensive study of pebbles from the 'Salento-type' allochthnous bauxite deposit (Otranto, southern Italy), originally derived from a pristine Campanian bauxite, has been performed for evaluating: 1) the chemical fractionation and inter-elemental relationships, especially for critical elements, 2) the climatic conditions that promoted bauxite formation, and 3) the provenance of the protolith(s) using zircon age data and conservative elemental proxies. The study confirms the capability of bauxite to concentrate many elements defined as critical by the European Union report on critical raw materials. Sc, Co, Ga, and especially Cr, are enriched when compared with the UCC composition and assuming Nb is immobile. Other critical elements such as the REEs, with the exception of La, are moderately depleted. R-mode factor analysis suggests that most of the variance in our chemical dataset is explained by a factor with significant weightings for TiO_2, Al_2O_3, Fe_2O_3, Sc, V, Nb, REEs, Pb and Th. This arises from climate effects affecting the distribution of the more abundant oxides and some trace elements, including the critical metals Nb and REEs. The texture of the pebbles is typical for Apulian karst bauxites and consists of sub-spheroidal ooids composed of boehmite and dispersed in a fine-grained matrix. The growth of the ooids, which formed under dry climate, was described in terms of fractal geometry. The average fractal dimension value of the ooids in the pebbles is close to that of the diffusion-limited aggregation models suggesting the ooid growth can be modelled using a molecular diffusion pattern, based on Fick's first law. The calculated time required for growth of the boehmite concretions is ~45 ÷ 310 ka. This finding is consistent with an intra-Campanian emersion event (74–76 Ma) that occurred during a dry and warm climatic stage. Since most of the karst bauxites worldwide have an ooidic texture, evaluation of the composition of concretions and the time required for their growth represents a powerful tool in reconstructing the palaeoenvironment. The zircon grains collected from the pebbles of the Salento-type karst bauxite define several concordant age populations. The youngest cluster, Early Cretaceous in age (99 ÷ 127.5 Ma), suggests that windborne particles from Cretaceous volcanics, possibly originating in the Carpatho-Balkan orogenic belts, provided material for further bauxitisation. The largest cluster (623 ÷ 689 Ma) is of Neoproterozoic age, predominately from the Late Ediacaran and Cryogenian p.p.. The 900–540 Ma Pan-African orogenic cycle was followed by continental-scale uplift and erosion, leading to the deposition of thick Cambrian–Ordovician siliciclastic sequences that represent the most widespread detrital sequence ever deposited on continental crust and that now cover large parts of North Africa. These Cambrian–Ordovician sandstones contain a large population of Neoproterozoic zircons of Cryogenian age. Neoproterozoic zircons also occur in the youngest (Silurian–Mesozoic) sandstones of the Saharan Metacraton. These sandstones also contain 1.0 Ga detrital zircons, suggesting as the oldest zircons found in the Salento-type bauxite pebbles (866 Ma and 941 Ma in age) are younger representatives of the zircon cluster present in this sandstone unit.

These zircon age determinations suggest that the source material for the Salento-type bauxite pebbles was a combination of magmatic material from a distant source and clastic material derived from a continental margin (North Africa). This result concurs with the Eu/Eu^* vs. Sm/Nd binary diagram, on which bauxite pebbles fall close to a mixing curve with andesite and cratonic sandstone end-members. As our results indicate that material was sourced from the North African continental margin, we suggest that a continental bridge separated oceanic domains in the Late Cretaceous of the Peri-Tethyan domain.

* Corresponding author.
E-mail address: giovanni.mongelli@unibas.it (G. Mongelli).

http://dx.doi.org/10.1016/j.oregeorev.2016.03.002
0169-1368/

1. Introduction

Bauxite deposits form in tropical to sub-tropical climates, and where they overlie carbonate units, regardless of the degree of karstification, they are referred to as karst bauxites (Bárdossy, 1982). The term 'Salento-type bauxite' refers to allochthonous deposits consisting of bauxitic debris that originated from the weathering and erosion of older deposits (Bárdossy, 1982).

Bauxite ores are commonly enriched in metals critical to industry, and the value of bauxite ore has increased with the limited supply of such metals (Vidal et al., 2013). The latest European Union report on critical raw materials (2014) listed many elements (e.g. Rare Earth Elements and Nb) usually found in karst bauxites (e.g. Mongelli et al., 2014 and references therein), thereby highlighting the importance of the world's bauxite resources (e.g. Mameli et al., 2007). There has been increasing demand for the economic elements found in bauxite ores, and their future availability is uncertain (Herrington, 2013); consequently, recent research has focused on the processes that control the distribution of economic elements in karst bauxite deposits (e.g. Abedini and Calagari, 2014; Boni et al., 2013; Hanilçi, 2013; Karadağ et al., 2009; Ling et al., 2015; Mameli et al., 2007; Mongelli et al., 2014; Peh and Kovačević Galović, 2014; Wang et al., 2010; Yu et al., 2014; Yuste et al., 2014; Zarasvandi et al., 2008). Whilst karst bauxites in southern Italy no longer have any economic value, they can be used as a valuable model for understanding similar deposits elsewhere in the world.

The importance of bauxite deposits is not restricted to providing a source of resources, as such deposits are also useful in addressing broader geological questions. Bauxite deposits worldwide formed mainly during the late Palaeozoic, the middle to Late Cretaceous, and the middle to late Cenozoic, as climatic and tectonic conditions at these times promoted prolonged periods of weathering (Meyer, 2004). Bauxite deposits can be grouped into provinces based on their geographic distribution. The southern European province is characterised by the presence of karst bauxites (Bogatyrev and Zhukov, 2009; Gow and Lozej, 1993). In southern Italy, which is part of the Peri-Tethyan realm, karst bauxite deposits often occur along local or regional unconformities associated with sub-aerial exposure events that occurred between the Cretaceous and the Eocene (Zarcone et al., 2010). One area of particular importance is the Apulia Carbonate Platform (ACP), which contains several Late Cretaceous autochthonous and allochthonous karst bauxite deposits.

Previous studies have examined the Cenomanian–Turonian autochthonous karst bauxite deposits of the ACP (Mongelli, 1997, 2002; Mongelli and Acquafredda, 1999). Based on elemental proxies the provenance of this bauxite deposit is thought to be the northern margin of the African continent (Mongelli et al., 2014). However, few data exist for the allochthonous 'Salento-type' karst bauxite of the ACP. This deposit consists of large pebbles that are the remnants of a pristine bauxite deposit. This source bauxite deposit likely formed during the middle Campanian (Mongelli et al., 2015), and thus may provide information on the evolution of the Peri-Tethyan realm during the Late Cretaceous.

Here we present, for the first time, a comprehensive study of the allochthonous Salento-type karst bauxite from the Otranto site, located on the southernmost part of the Salento Peninsula, southern Italy. The study is based on image analysis and textural observations, bulk mineralogical and chemical compositions, micro-chemical determinations, and radiometric dating of detrital zircons. The aims are: 1) to assess chemical fractionation and inter-elemental relationships, especially for critical elements; 2) to evaluate the climatic conditions that promoted bauxite formation in this region and the duration of such conditions; and 3) to estimate the provenance of the protolith(s) using elemental proxies and zircon age data.

2. Geological setting

The study area is part of the complex structural framework of the Central Mediterranean, one of numerous oceanic domains that have formed the Tethys Ocean since the Permian (Vrielynck et al., 1996).

The geodynamic evolution of the Tethys was constrained by the movements of the Africa and Eurasia cratons since the Jurassic (Schettino and Turco, 2011), and was further complicated by the complex orogenic history of the whole Tethyan realm. The Africa and Eurasia cratons have been converging since the Late Cretaceous (Dewey et al., 1989), impacting on a number of small peri-Adriatic carbonate platforms (*sensu* Zappaterra, 1994) of the Adria plate. Several studies (Channell, 1996; Dercourt et al., 2000; Finetti, 2005; Stampfli, 2000) have focused on the geodynamics of the Tethys during the Mesozoic; however, uncertainties remain about the relationship between the Adria and African plates. Two main palaeotectonic models have been proposed: 1) Adria was an independent microplate, whereby the Ionian Tethys and Alpine Tethys oceanic domains were connected, separating the Adria microplate from the African plate; and 2) Adria was part of the African Promontory, with the two oceanic domains being separated by continental crust that Bosellini (2002) and Zarcone et al. (2010) referred to the Panormide Carbonate Platform.

The ACP is a peri-Adriatic platform that developed on the southern margin of the Tethys Ocean. It represents part of the foreland basin of both the Apennine and Dinaric thrust-and-fold belts (Fig. 1). This platform consists mainly of Upper Triassic–Upper Cretaceous shallow-marine carbonates (Bernoulli, 2001; Bosellini, 2004) accumulated over a continental crust basement and overlain by thin carbonate and terrigenous successions of Neogene–Quaternary age (Ciaranfi et al., 1992; Ricchetti et al., 1992). Bauxite deposits, palaeokarsts and palaeosoils are common in the ACP carbonate succession, suggesting several sub-aerial exposure events presumably related to local factors (e.g. platform subsidence or tectonic control) as much as global factors (eustatic sea-level change, intraplate response to distant subduction or collision processes, Mindszenty et al., 1995).

In this study, we focus on Salento-type bauxite deposits outcropping at Otranto (southern Italy, Central Mediterranean, Fig. 1), where a wide section of the APC is exposed. This section consists of bauxitic debris deposits that overlie heavily weathered Upper Cretaceous limestone and are overlain by a Upper Oligocene continental succession consisting of sediments formed in alternating freshwater, lagoonal and emergent environments (Fig. 2; Esu and Girotti, 2010). The Otranto bauxite is several metres thick, reddish-yellowish in colour, and contains many large bauxite pebbles that are remnants of an original source bauxite deposit, embedded in a clayey matrix (Esu and Girotti, 2010). Mongelli et al. (2015) suggested that the original source bauxite formed during a middle Campanian (74–76 Ma) emersion event, possibly related to a tectonic uplift (Morsilli and Rustichelli, 2004) and/or to a sea level lowstand (Cloething and Haq, 2015; Haq, 2014). Its formation is correlated with sub-aerial exposure recorded on the Adriatic island of Brač (Schlűter et al., 2008; Steuber et al., 2005) and corresponds to a sequence boundary dated at 75.6 Ma in the Boreal seaway of Europe and North America (Hardenbol and Vail, 1998), consistent with the 'Upper Campanian event' of Jarvis et al. (2002).

3. Sampling and methods

We collected 20 samples from the Salento-type deposit at the Otranto site, with each sample consisting of several well-preserved bauxite pebbles of ~10 cm in diameter. The samples were first dried and then manually milled in an agate mortar to generate a very fine powder suitable for chemical and mineralogical analysis. Whole-rock mineralogy was determined using X-ray powder diffraction (XRPD). XRPD was performed at the Department of Sciences, University of Basilicata, Italy, using a Philips X'Pert PW3040 powder diffractometer

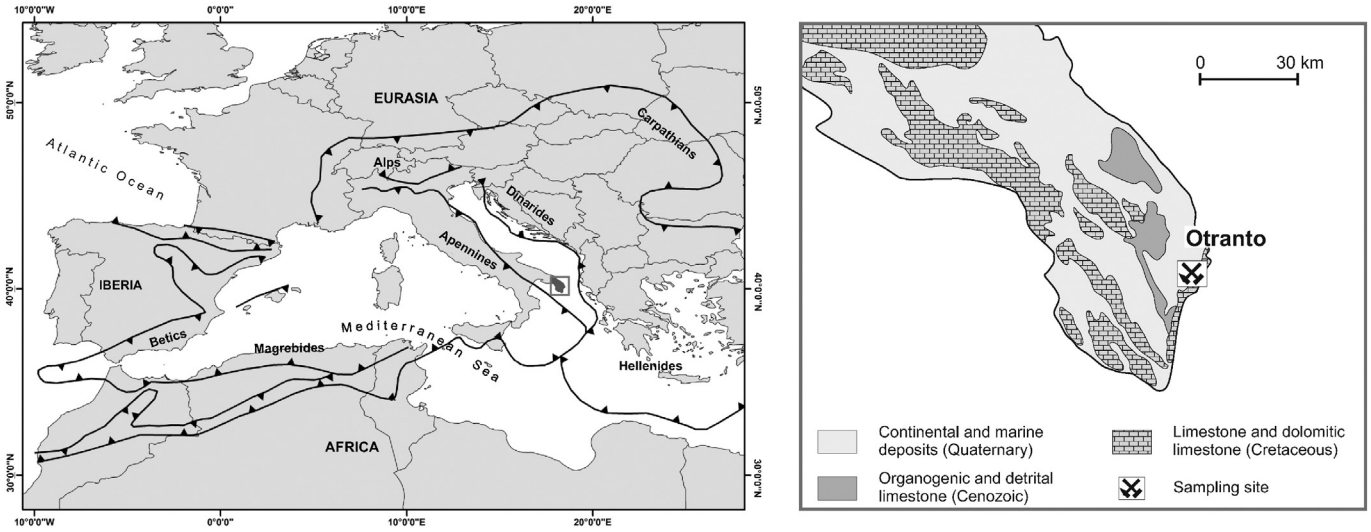

Fig. 1. Simplified present-day tectonic sketch of the Mediterranean area where the main subduction zones and location of the study area are shown. Geological sketch map (right) of the Salento peninsula (southern Italy) is also displayed.

with Cu-Kα radiation and settings of 40 kV, 30 mA, and 0.02° (2θ). Chemical compositions were determined by ICP and ICP–MS analyses at Activation Laboratories (Ancaster, Canada). Powdered samples were digested using a four acid attack (HF, HNO_3, $HClO_4$, and HCl). Using this method, a 0.25 g sample is first digested using hydrofluoric acid. The sample is then treated in a mixture of nitric and perchloric acids before being heated in several ramping and holding cycles, using precise programmer-controlled heating, taking the samples to incipient dryness. Next, the samples are brought back into solution using aqua regia before being analysed using a Varian ICP and a PerkinElmer Sciex ELAN 9000 ICP-MS. Analytical uncertainties for this method are less than ±5%, except for elements at concentrations of ≤10 ppm which have uncertainties of ±5–10%. Total loss on ignition (LOI) values were gravimetrically estimated after overnight heating at 950 °C.

Elemental mobility for trace elements was estimated using an absolute weathering index (Nesbitt, 1979), with the assumption that Nb was immobile during bauxitisation (Mongelli et al., 2014) and using an average Upper Continental Crust (UCC; Taylor and McLennan, 1985) composition as the parental material. Percentage changes are expressed as $[(E_{sample} / Nb_{sample}) / (E_{UCC} / Nb_{UCC}) - 1] \times 100$, where E is the concentration of the selected element.

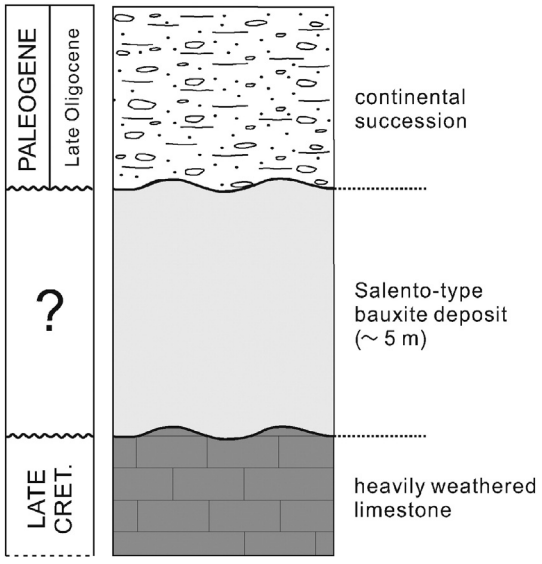

Fig. 2. Stratigraphic column of the Otranto sampling site. Thicknesses are not in scale.

Micromorphological and microchemical analyses were undertaken using an environmental scanning electron microscopy (ESEM). We employed an XL30 Philips LaB_6 ESEM instrument equipped with an energy dispersive X-ray spectrometer (SEM–EDS) at the Microscopy Laboratory of the Department of Sciences, University of Basilicata, Italy, and a Fei/Philips FEG Quanta 200 at the Earth Sciences Department, University of Calabria, Italy.

Image analyses were performed on slabs (4.5 x 2.5 cm) using the free software ImageJ. Binarization of each sample image was used to obtain a double colour image (ooids in black and matrix in white). We then measured the ooid-to-matrix ratio, determined by calculating the percentage of the total area occupied by ooids, and observed the major geometric features of the ooids observed in thin section, including circularity and aspect ratio. We performed fractal analysis using the automatic box counting technique, breaking the image into boxes of decreasing size and measuring the number of boxes filled by ooids (filling frequency) for each size class. The fractal dimension D as then calculated as the slope of the line of best fit for the natural logarithm of the filling frequency versus the natural logarithm of the box size.

For analyses of zircons, ~20 kg of bauxite was first crushed (to <250 μm) and then zircon crystals were separated at the Department of Biological, Geological and Environmental Sciences of the University of Bologna 'Alma Mater', using standard hydrodynamic, magnetic and heavy liquid separation techniques. To ensure we captured all zircon crystals, we then hand-picked crushed samples under a binocular microscope. Zircon grains were set in epoxy resin mounts, sectioned and polished. Prior to analysis, backscatter electron micrographs were obtained using SEM. We used these SEM micrographs to examine the morphology and internal structure of zircons to help select sites (without inclusions and fractures) suitable for subsequent analysis.

U–Pb zircon ages were determined using a 193 nm ArF excimer laser ablation (LA) microprobe (Microlas GeoLas 200Q) coupled to a magnetic sector ICP–MS (inductively coupled plasma–mass spectrometer; Element 1 from Thermo Finnigan) at IGG-CNR (Pavia, Italy). The U–Pb analyses were performed in single spot mode, with a spot size of 10–20 μm. The laser frequency was 5 Hz and we used a fluence of 12 Jcm^{-2}. Sixty seconds of background signal and at least 30 s of ablation signal were acquired for each zircon. The following mass spectra were acquired in magnetic scanmode: ^{202}Hg, $^{204}(Pb + Hg)$, ^{206}Pb, ^{207}Pb, ^{208}Pb, ^{232}Th and ^{238}U. The proportion of ^{235}U was calculated

from ^{238}U values, using the ratio $^{238}U/^{235}U = 137.88$ (Tiepolo, 2003). The ^{202}Hg and ^{204}Hg masses were measured to identify the presence of common Pb in the zircons, and the signal of ^{202}Hg was used to correct the isobaric interference of ^{204}Hg on ^{204}Pb (Horn et al., 2000). The relatively high Hg background values prevented the detection of low-^{204}Pb signals. For all of the analysed zircons we detected signals of 204 mass, indistinguishable from background. Because of this, no common Pb correction was applied and the $^{206}Pb/^{204}Pb$ ratio is not reported (for further details, see Tiepolo, 2003). Mass bias and laser-induced fractionation were corrected by adopting zircon 91500 (1062.4 ± 0.4 Ma; Wiedenbeck et al., 1995) as an external standard. During each analytical reference run, zircon 02123 (295 Ma; Ketchum et al., 2001) was analysed together with unknowns for quality control. Data reduction was performed using the GLITTER software package (van Achterbergh et al., 2001). Time-resolved signals were carefully inspected to detect perturbation of the signal due to inclusions, cracks or mixed-age domains. Within the same analytical run, the error associated with the reproducibility of the external standards was propagated to each analysis of the sample (see Horstwood et al., 2003). After this procedure, each age determination was retained, accurate to within the quoted error.

4. Results

4.1. Geochemistry and mineralogy

Table 1 lists the chemical compositions (including major, trace and rare earth element concentrations) and elemental ratios of the examined bauxite pebbles. The pebbles of the Salento-type karst bauxite are composed mainly of three major oxides: Al_2O_3 (average = 58.40 ± 1.80 wt.%), Fe_2O_3 (average = 20.34 ± 1.85 wt.%),

Table 1
Major, trace and rare earth element concentrations of the Otranto bauxite pebbles.

	OT1	OT2	OT3	OT4	OT5	OT6	OT7	OT8	OT9	OT10	OT11	OT12	OT13	OT14	OT15	OT16	OT17	OT18	OT19	OT20
wt.%																				
SiO_2	0.96	0.95	0.44	1.10	0.96	0.90	0.92	0.90	0.85	0.92	0.56	0.86	0.86	0.89	0.84	0.94	0.95	0.91	0.45	0.48
Al2O3	56.82	57.58	59.70	54.50	54.67	57.59	58.80	59.62	62.13	58.47	58.84	58.68	58.73	58.17	59.13	58.47	59.15	56.94	61.16	58.81
Fe2O3(T)	21.57	20.70	18.01	23.74	23.80	21.47	19.34	19.34	16.77	19.91	20.10	20.13	20.03	20.79	18.07	21.14	20.14	23.36	19.07	19.25
MnO	0.16	0.15	0.15	0.21	0.19	0.17	0.15	0.15	0.15	0.15	0.15	0.15	0.15	0.16	0.15	0.15	0.15	0.17	0.17	0.18
MgO	0.17	0.16	0.17	0.18	0.16	0.15	0.16	0.17	0.17	0.15	0.15	0.15	0.15	0.17	0.18	0.15	0.15	0.14	0.16	0.16
CaO	0.87	0.68	0.87	0.69	0.53	0.52	0.43	0.34	0.85	0.20	0.15	0.15	0.18	0.68	0.89	0.13	0.13	0.13	0.08	0.08
Na2O	0.01	0.01	0.01	0.02	0.01	0.01	0.01	0.01	0.02	0.01	bdl	0.02	0.01	0.01	0.01	0.01	0.01	0.01	bdl	bdl
K2O	bdl	bdl	bdl	bdl	bdl	bdl	bdl	bdl	bdl	bdl	bdl	bdl	bdl	bdl	bdl	bdl	bdl	bdl	bdl	bdl
TiO2	2.48	2.83	2.80	2.49	2.49	2.59	2.85	2.96	2.96	2.56	2.59	2.63	2.57	2.61	2.73	2.69	2.72	2.45	2.54	2.46
P2O5	0.05	0.05	0.04	0.05	0.06	0.05	0.05	0.03	0.05	0.06	0.05	0.05	0.05	0.05	0.04	0.05	0.05	0.05	0.04	0.07
LOI	15.71	16.13	16.44	15.59	15.80	15.61	16.36	16.61	16.64	16.14	16.95	15.86	15.95	15.99	16.46	16.24	16.46	16.10	16.61	16.77
Total	98.79	99.24	98.64	98.55	98.67	99.04	99.07	100.10	100.60	98.57	99.53	98.67	98.67	99.50	98.51	99.95	99.90	100.30	100.30	98.26
ppm																				
Sc	45	43	43	53	48	44	43	43	41	43	44	44	42	45	42	46	44	50	45	45
V	223	207	196	239	222	209	192	189	183	196	219	201	190	215	188	203	195	219	219	222
Cr	1060	1010	920	930	960	1040	1020	1020	940	1110	1020	980	1000	960	920	1070	1050	1130	930	920
Co	37	35	136	56	42	32	47	43	142	34	36	32	39	79	61	34	34	41	31	32
Ni	150	160	310	190	170	140	180	190	290	170	220	150	170	210	190	170	160	170	210	210
Cu	40	50	60	60	60	50	60	50	60	60	60	50	50	50	50	50	50	60	70	70
Zn	230	260	270	240	250	260	300	280	250	280	290	250	270	250	240	290	300	240	280	280
Ga	56	58	67	52	52	54	60	60	57	60	68	54	57	53	53	58	59	55	67	67
As	46	32	64	46	44	38	34	31	41	32	77	36	39	46	37	33	31	40	69	70
Sr	62	59	66	59	55	55	54	55	62	47	53	48	48	59	61	49	50	46	49	49
Y	52	53	57	60	56	55	52	54	56	53	57	53	53	54	52	56	55	61	56	57
Zr	539	547	552	592	550	535	550	561	536	521	574	544	523	537	533	550	555	553	576	570
Nb	70	74	80	71	69	73	78	80	80	77	78	74	77	75	74	76	80	71	71	74
Mo	7	7	8	9	7	7	7	7	6	7	9	7	7	6	6	7	7	6	7	7
Ba	17	17	15	17	16	16	17	18	19	16	14	16	16	17	17	17	17	15	13	14
Hf	12.2	12.0	11.1	13.7	12.6	12.5	12.0	12.5	12.1	12.1	12.7	12.2	12.8	12.1	11.5	11.9	11.6	11.8	11.4	12.2
Pb	103	72	71	146	123	110	78	73	87	79	91	95	98	102	84	71	64	102	110	124
Th	50.2	40.3	37.5	61.8	55.6	50.2	41.7	39.6	33.6	45.3	51.0	48.2	49.6	46.1	41.6	38.1	35.9	51.9	63.0	68.8
U	5.5	5.4	37.9	10.7	6.4	6.0	8.4	6.8	42.1	5.9	5.7	5.4	5.4	16.4	14.1	6.1	5.6	5.2	5.8	5.6
La	99.1	84.5	84.3	129.0	111.0	97.5	81.7	79.0	77.2	86.6	96.4	91.8	96.7	91.6	79.3	93.6	86.4	108.0	117.0	127.0
Ce	157	123	152	204	163	161	132	130	147	135	146	141	148	156	139	134	126	143	145	152
Pr	16.0	13.7	14.7	20.2	17.3	15.7	13.5	13.1	13.1	14.4	16.3	14.3	15.3	14.4	12.9	14.7	13.3	17.3	18.3	19.8
Nd	57.8	48.7	53.3	71.5	63.5	55.5	49.1	48.8	50.0	51.7	59.4	51.2	54.6	53.6	46.6	53.1	51.1	61.8	65.2	70.0
Sm	11.0	9.7	10.7	13.8	11.4	11.2	10.1	9.4	10.0	10.5	11.2	9.9	10.4	10.1	9.3	10.9	9.9	12.0	12.2	12.3
Eu	2.4	2.1	2.3	2.9	2.4	2.4	2.1	2.2	2.1	2.3	2.4	2.1	2.3	2.1	1.9	2.3	2.3	2.5	2.5	2.6
Gd	8.5	7.9	8.6	10.5	8.7	8.6	7.8	7.7	7.8	8.3	8.9	7.7	8.1	8.1	7.3	8.6	8.6	9.7	9.7	10.0
Tb	1.6	1.3	1.6	1.8	1.5	1.5	1.4	1.4	1.4	1.5	1.5	1.5	1.5	1.5	1.3	1.5	1.4	1.6	1.7	1.7
Dy	9.4	8.5	9.5	10.6	9.5	8.7	8.5	8.5	9.3	9.3	9.5	8.5	9.0	8.7	8.1	9.1	8.6	9.8	9.4	9.9
Ho	1.9	1.8	2.0	2.2	2.0	2.0	1.9	1.8	1.9	1.9	2.0	1.8	2.0	1.9	1.7	1.9	1.9	1.9	1.9	2.0
Er	5.8	5.5	6.1	6.6	5.9	5.7	5.8	5.7	5.6	5.7	6.0	5.5	5.6	5.5	5.3	5.7	5.6	5.9	6.1	6.1
Tm	1.0	0.9	1.0	1.1	1.0	1.0	1.0	1.0	1.0	0.9	1.0	0.9	1.0	0.9	0.9	1.0	1.0	1.0	1.0	1.0
Yb	6.5	6.2	6.5	6.9	6.4	6.1	6.5	6.3	6.7	6.1	6.7	6.2	6.4	6.4	5.8	6.5	6.1	6.6	6.4	6.5
Lu	0.9	0.9	1.0	1.1	0.9	0.9	0.9	0.9	1.0	0.9	0.9	0.9	0.9	0.9	0.8	0.9	0.9	0.9	0.9	1.0
REE	378.9	314.7	353.6	482.2	404.5	377.7	322.3	315.7	334.1	335.1	368.3	343.3	361.9	361.7	320.2	343.8	323.1	382.0	397.3	421.9
Ce/Ce*	0.79	0.73	0.89	0.79	0.73	0.83	0.80	0.81	0.94	0.77	0.75	0.77	0.77	0.85	0.87	0.72	0.73	0.66	0.62	0.60
Eu/Eu*	0.74	0.73	0.75	0.74	0.74	0.73	0.73	0.78	0.73	0.74	0.74	0.73	0.78	0.71	0.71	0.72	0.75	0.71	0.71	0.72
(La/Yb)ch	10.30	9.21	8.76	12.63	11.72	10.80	8.49	8.47	7.79	9.59	9.72	10.01	10.21	9.67	9.24	9.73	9.57	11.06	12.35	13.20
Sm/Nd	0.19	0.20	0.20	0.19	0.18	0.20	0.21	0.19	0.20	0.20	0.19	0.19	0.19	0.19	0.20	0.21	0.19	0.19	0.19	0.18

Note: b.d.l. = below detection limit.

Table 2
Change % values of the Otranto bauxite pebbles relatively to the Upper Continental Crust composition

	OT1	OT2	OT3	OT4	OT5	OT6	OT7	OT8	OT9	OT10	OT11	OT12	OT13	OT14	OT15	OT16	OT17	OT18	OT19	OT20
Sc	46.1	32.1	22.2	69.7	58.1	37.0	25.3	22.2	16.5	26.9	28.2	35.1	24.0	36.4	29.0	37.6	25.0	60.1	44.0	38.2
V	32.7	16.6	2.1	40.3	34.1	19.3	2.6	−1.6	−4.7	6.1	17.0	13.2	2.8	19.4	5.9	11.3	1.6	28.5	28.5	25.0
Cr	981.6	874.9	721.4	835.6	893.8	917.6	834.1	810.7	739.3	929.7	834.1	845.9	827.6	814.3	788.0	905.6	837.5	1036.8	835.6	788.0
Co	32.1	18.2	325.0	97.2	52.2	9.6	50.6	34.4	343.8	10.4	15.4	8.1	26.6	163.3	106.1	11.8	6.3	44.4	9.2	8.1
Ni	167.9	170.3	384.4	234.5	208.0	139.7	188.5	196.9	353.1	176.0	252.6	153.4	176.0	250.0	220.9	179.6	150.0	199.3	269.7	254.7
Cu	−42.9	−32.4	−25.0	−15.5	−13.0	−31.5	−23.1	−37.5	−25.0	−22.1	−23.1	−32.4	−35.1	−33.3	−32.4	−34.2	−37.5	−15.5	−1.4	−5.4
Zn	15.7	23.7	18.8	19.0	27.6	25.4	35.4	23.2	10.0	28.0	30.9	19.0	23.5	17.4	14.2	34.4	32.0	19.0	38.9	33.2
Ga	17.6	15.3	23.2	7.7	10.8	8.8	13.1	10.3	4.8	14.6	28.2	7.3	8.9	3.9	5.3	12.2	8.5	13.9	38.8	33.1
As	995.2	620.7	1233.3	979.8	962.8	767.6	626.5	545.8	754.2	592.6	1545.3	710.8	744.2	922.2	733.3	623.7	545.8	839.0	1519.7	1476.6
Sr	−93.7	−94.3	−94.1	−94.1	−94.3	−94.6	−95.1	−95.1	−94.5	−95.6	−95.1	−95.4	−95.5	−94.4	−94.1	−95.4	−95.5	−95.4	−95.1	−95.3
Y	−15.6	−18.6	−19.0	−4.0	−7.8	−14.4	−24.2	−23.3	−20.5	−21.8	−17.0	−18.6	−21.8	−18.2	−20.1	−16.3	−21.9	−2.4	−10.4	−12.5
Zr	1.3	−2.7	−9.2	9.7	4.9	−3.6	−7.2	−7.7	−11.8	−11.0	−3.2	−3.3	−10.6	−5.8	−5.2	−4.8	−8.7	2.5	6.7	1.4
Mo	66.7	57.7	66.7	111.3	69.1	59.8	49.6	45.8	25.0	51.5	92.3	57.7	51.5	33.3	35.1	53.5	45.8	40.8	64.3	57.7
Ba	−98.9	−99.0	−99.1	−98.9	−98.9	−99.0	−99.0	−99.0	−98.9	−99.1	−99.2	−99.0	−99.1	−99.0	−99.0	−99.0	−99.0	−99.0	−99.2	−99.1
La	18.0	−4.8	−12.2	51.4	34.1	11.3	−12.7	−17.7	−19.6	−6.3	3.0	3.4	4.7	1.8	−10.7	2.6	−10.0	26.8	37.3	43.0
Ce	−12.4	−35.1	−25.8	12.2	−7.7	−13.8	−33.9	−36.5	−28.2	−31.5	−26.9	−25.6	−24.9	−18.8	−26.6	−31.1	−38.5	−21.3	−20.2	−19.8
Pr	−19.5	−34.8	−35.3	0.2	−11.7	−24.3	−39.1	−42.3	−42.3	−34.2	−26.4	−32.0	−30.0	−32.4	−38.6	−31.9	−41.5	−14.2	−9.2	−5.8
Nd	−20.6	−36.7	−35.9	−3.2	−11.5	−26.9	−39.5	−41.3	−39.9	−35.4	−26.8	−33.5	−31.8	−31.3	−39.4	−32.8	−38.6	−16.3	−11.7	−9.0
Sm	−12.7	−27.2	−25.7	8.0	−8.2	−14.8	−28.1	−34.7	−30.6	−24.2	−20.2	−25.7	−25.0	−25.2	−30.2	−20.3	−31.3	−6.1	−4.5	−7.7
Eu	−4.6	−19.8	−16.9	17.2	−0.4	−8.5	−22.4	−22.9	−24.7	−16.2	−12.2	−20.1	−13.7	−20.1	−26.3	−14.8	−19.4	0.8	0.4	1.0
Gd	−20.1	−29.8	−29.3	−2.7	−17.0	−22.5	−34.2	−36.7	−35.9	−29.1	−24.9	−31.5	−30.8	−28.9	−35.1	−25.6	−29.3	−10.1	−10.1	−11.1
Tb	−10.7	−31.4	−21.9	−1.0	−15.1	−19.7	−29.9	−31.6	−31.6	−23.9	−24.9	−20.8	−23.9	−21.9	−31.4	−22.9	−31.6	−12.0	−6.5	−10.3
Dy	−4.1	−18.0	−15.2	6.6	−1.7	−14.9	−22.2	−24.1	−17.0	−13.7	−13.0	−18.0	−16.5	−17.1	−21.8	−14.5	−23.2	−1.4	−5.4	−4.4
Ho	−15.2	−24.0	−21.9	−3.2	−9.4	−14.4	−23.9	−29.7	−25.8	−22.9	−19.9	−24.0	−18.8	−20.8	−28.2	−21.9	−25.8	−16.4	−16.4	−15.5
Er	−9.9	−19.2	−17.1	1.0	−7.1	−15.1	−19.2	−22.6	−23.9	−19.5	−16.4	−19.2	−20.9	−20.3	−22.2	−18.5	−23.9	−9.7	−6.6	−10.4
Tm	7.1	−4.8	−5.3	15.2	7.6	−1.4	−5.8	−10.0	−9.1	−8.5	−0.9	−6.8	−2.6	−6.1	−9.9	0.7	−9.1	5.6	4.6	4.4
Yb	5.5	−4.8	−7.7	10.4	5.4	−5.0	−5.3	−10.5	−4.8	−10.0	−2.4	−4.8	−5.5	−3.0	−10.9	−2.8	−13.4	5.6	2.4	−0.2
Lu	4.9	−9.2	−3.3	18.8	5.3	−6.9	−6.9	−11.1	−5.3	−7.7	−5.8	−8.2	−4.6	−8.3	−11.3	−5.4	−10.2	2.3	3.4	2.4
Hf	−24.9	−30.1	−40.2	−16.8	−21.3	−26.2	−33.7	−32.7	−34.8	−32.3	−29.8	−28.9	−28.3	−30.5	−33.0	−32.5	−37.5	−28.4	−30.8	−28.9
Pb	83.9	21.6	10.9	157.0	122.8	88.4	25.0	14.1	35.9	28.2	45.8	60.5	59.1	70.0	41.9	16.8	0.0	79.6	93.7	109.5
Th	67.6	27.2	9.5	103.4	88.3	60.7	24.9	15.7	−1.9	37.5	52.8	52.2	50.5	43.6	31.3	17.1	4.8	70.8	107.3	117.2
U	−29.8	−34.8	323.0	34.6	−17.2	−26.6	−3.8	−24.1	369.9	−31.6	−34.8	−34.8	−37.4	95.2	70.1	−28.3	−37.5	−34.6	−27.1	−32.4

and TiO_2 (average = 2.65 ± 0.16 wt.%). The SiO_2 content is generally <1 wt.%.

The percentage changes of trace elements are given in Table 2 and displayed in Fig. 3. As expected, the large ion lithophile elements (LILEs; e.g. Sr and Ba) are strongly depleted relative to Nb, with average percentage changes close to −100%, whereas Pb is enriched, with an average change of +58.2%. Transition metals, with the exception of Cu (−25.9%), are all enriched relative to Nb. Percentage changes for Sc, V, Cr, Co, Ni and Zn vary between +15.0% (V) and greater than +800% (Cr). Three of these elements (Sc, Cr and Co) are critical metals, based on a European Union report on critical raw metals (2014). Results for another critical metal, Ga, show a change of +14.3%. Rare earth elements, divided into light REEs (LREEs: La to Sm) and heavy REEs (HREEs: Eu to Lu), are also critical metals and are generally moderately depleted relatively to Nb. Changes in LREEs range from a +7.2% for La to −28.1% for Nd. Changes for HREEs range from −1.8% for Tm to −24.7% for Gd. The high field strength elements (HFSEs) Y (−16.4%), Zr (−3.4%) and Hf (−30.1%) are depleted relative to Nb, whereas Th (+49.0%), Mo (+56.8%) and As (+887.0%) are enriched relative to Nb.

The chondrite-normalised REE patterns for the bauxite pebbles are shown in Fig. 4 (reference chondrite values are from Evensen et al., 1978). Total REE (ΣREE) concentrations range from 314.7 to 482.2 ppm (average = 362.1 ± 42.0 ppm). The REEs are moderately fractionated, with $(La/Yb)_{ch}$ ratios of 7.79 ± 13.20 (average = 10.13 ± 1.45). The samples have moderately negative Ce anomalies, with Ce/Ce^* ratios of 0.60–0.94 (average = 0.77 ± 0.08), and all the samples have uniformly negative Eu anomalies of 0.71–0.78 (average = 0.74 ± 0.02). Whole-rock mineralogical analyses show that the bauxite pebbles consist mainly of boehmite with minor iron oxyhydroxides (hematite and goethite), and anatase consistent with Mongelli et al. (2015).

4.2. Texture and geometrical features

The bauxite pebbles consist of sub-spheroidal textural components (ooids) dispersed in a fine-grained matrix. The ooids are formed of boehmite (Fig. 5) and in some cases have a thin rim of Al-hematite. Iron-rich layers are likely second-generation iron oxide, composed of goethite that formed by the breakdown of boehmite during erosion and weathering of the source bauxite beds (Delvigne, 1998). This second-generation iron oxide occurs in the cores of ooids as micro-domains, and locally replaces almost all of the boehmite in the core, as also reported by Mongelli et al. (2015).

Results of image analyses (Table 3) show that the ooid/matrix ratio is low (average = 0.13 ± 0.07). The average size of the boehmite ooids, based on measurements of 623 undeformed or weakly deformed particles from nine selected samples, is 46.2 μm (±20.6). The average

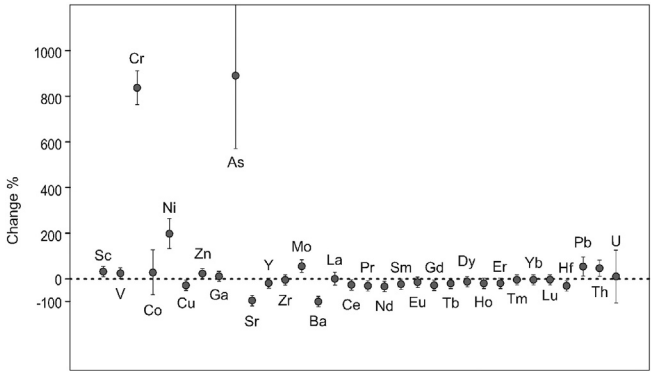

Fig. 3. Percentage changes of trace element concentrations relatively to the UCC composition and assuming Nb as immobile element. Average values (black circles) and standard deviation (thin vertical lines) are displayed. See the text for further details.

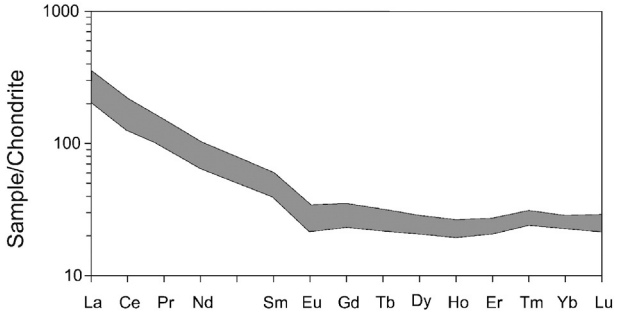

Fig. 4. Chondrite-normalized patterns of rare earth element concentrations.

circularity of the ooids (a dimensionless value ranging from 0 and 1, where 1 corresponds to a perfect circle) is 0.82 ± 0.03. The average aspect ratio (i.e. the ratio of the major axis to minor axis ratio, with a minimum value of 1 for circular particles) is 1.65 ± 0.09. The average fractal dimension D was 1.59 ± 0.1.

4.3. Zircon morphology and age data

Despite crushing 20 kg of material, only 12 zircon grains (30–100 μm in size) were recovered. The crystals vary in shape and zoning (Fig. 6). The various zoning patterns are as follows: a) magmatic zoning: zircons ZrS1, ZrS2, ZrS6, ZrS10 and ZrS12 show oscillatory zoning, characteristic of magmatic growth; b) xenocrystic cores: zircon ZrS10 has a core that is surrounded by magmatic oscillatory zoning, and the core is discordant with a magmatic overgrowth and is likely the remnant of older oscillatory zoning; c) secondary textures: the zircons commonly show perturbation of the original magmatic oscillatory zoning, especially in the crystal margins. This is particularly prominent for ZrS2, which contains a domain of patchy zoning.

The results of U–Pb zircon dating (Table 4, Fig. 7) show that four crystals (ZrS1 to ZrS4) are Cretaceous in age, as they yield concordant ages of 99, 99.5, 112.4, and 127.5 Ma, respectively. ZrS5 yields a concordant age of 315 Ma. The older Proterozoic zircon crystals are seven in total. Five of them (ZrS6-7-8-9-10) yield concordant ages of 623, 626, 642, 643, 662, and 689 Ma, respectively (ZrS6 has two analyses spot). The two oldest zircons (ZrS11 and ZrS12) yield concordant ages of 866 and 941 Ma, respectively.

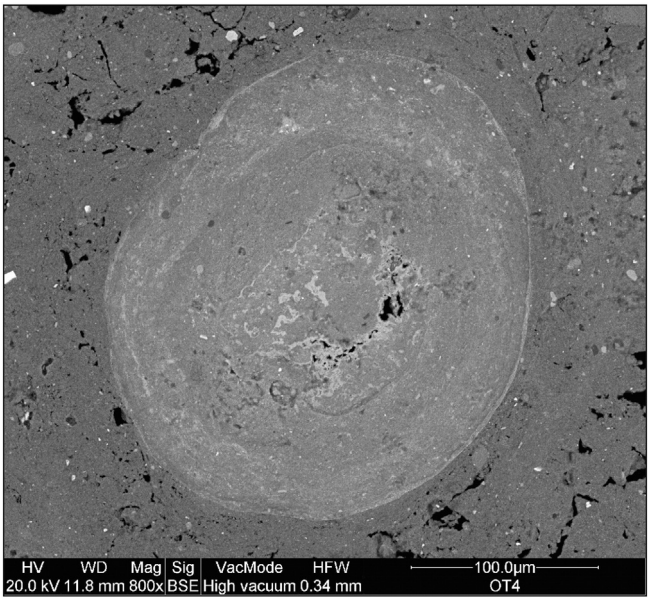

Fig. 5. Back-scattered electron image of a boehmite ooid of pebbles from the Otranto bauxite.

Table 3
Results of image analysis on the Otranto bauxite pebbles. Numbers are average values for each sample. See text for further details

	Circularity	Aspect ratio	D	ooids/matrix ratio
OT 1	0.83	1.54	1.38	0.04
OT 2	0.79	1.77	1.51	0.08
OT 3	0.76	1.93	1.39	0.05
OT 4	0.79	1.66	1.59	0.04
OT 5	0.80	1.58	1.69	0.11
OT 6	0.81	1.62	1.65	0.14
OT 7	0.88	1.66	1.54	0.11
OT 8	0.84	1.71	1.60	0.12
OT 9	0.83	1.67	1.72	0.28
OT10	0.79	1.57	1.68	0.07
OT11	0.81	1.69	1.48	0.12
OT12	0.85	1.7	1.61	0.09
OT13	0.83	1.61	1.54	0.17
OT14	0.8	1.65	1.65	0.25
OT15	0.78	1.57	1.7	0.12
O716	0.85	1.62	1.65	0.11
OT17	0.83	1.6	1.66	0.15
OT18	0.84	1.67	1.59	0.19
OT19	0.81	1.64	1.61	0.1
OT20	0.84	1.62	1.62	0.21
Average	0.82	1.65	1.59	0.13
Std. Dev.	0.03	0.09	0.10	0.07
Median	0.82	1.65	1.61	0.12

5. Discussion

5.1. Inter-elemental relationships

We performed R-mode factor analysis to evaluate inter-elemental relationships among TiO_2, Al_2O_3, and Fe_2O_3; the critical elements Cr, Co, Ga, Nb, and REEs; the transition metals Sc, V, Ni, Cu, and Zn; and the high field strength elements Zr, Hf, Th, and Pb.

Factors were extracted following Varimax rotation using the STATGRAPHICS Centurion XVI.I package. We used a standardised correlation matrix, thereby weighting all variables equally during factor calculations. The computed communalities provide an index of the efficiency of the proposed set of factors (Davis, 1986), and the magnitude of the communalities suggests that most of the original variance is accounted for by the chosen factors.

Three factors explain 88.6% of the total variance in the geochemical data (Table 5). The first factor (F1; Var. = 52.6%) includes significant and positive weightings for Fe_2O_3, Sc, V, REEs, Pb, and Th, and negative weightings for Al_2O_3, TiO_2, and Nb. Boehmite in the Apulian karst bauxites formed during dry climatic conditions whereas iron oxy-hydroxides formed during wet conditions (e.g. Mongelli et al., 2015, and references therein). Iron oxy-hydroxides formed both during the bauxitisation process, as thin hematite rims locally associated with ooids, and during erosion/weathering of the source bauxite deposit, either as goethite microdomains formed by the breakdown of the large boehmite ooid cores, or as microlayers within the matrix (Mongelli et al., 2015). Iron oxy-hydroxides may contain large amounts of trivalent vanadium (Kabata-Pendias, 2011), and trivalent scandium commonly co-occurs with Fe^{3+} (Brookins, 1988). It is therefore not surprising to find co-variance among Sc, V, and Fe_2O_3 in F1. Positive weightings for REEs, Th, and Pb are attributed to the accumulation, during wetter periods (i.e. during iron oxy-hydroxide formation), of tiny weathering-resistant crystals of monazite and xenotime, possibly deposited by dry wash. Drier conditions promote, in addition to the accumulation of Al_2O_3, also that of Ti and Nb, which share very similar geochemical behaviour. F1 therefore explains the effects of climate on the distribution of the more abundant oxides and on some trace elements, including the critical metals Nb and REEs.

The second factor (F2) explains 22.8% of the total variance within the dataset, and has significant and positive weightings for Ni and Co, and a significant and negative weighting for Cr. During weathering, transition metals are mildly soluble (e.g. Gaillardet et al., 2003) and the solubility of Ni^{2+} and Co^{2+} in the metal–O–H system under mildly alkaline to acidic conditions throughout the whole Eh range is well established. Consequently, these elements are available for adsorption onto secondary minerals (e.g. Smith, 1999). The release of Cr into aqueous solution usually requires oxidation to Cr^{6+} since most of the Eh–pH space is occupied by insoluble trivalent chromium in the form of Cr_2O_3 (e.g. Margiotta et al., 2012). F2 therefore represents differences in behaviour between the divalent transition metal cations and chromium when in surface environments.

The third factor (F3) explains 13.2% of the total variance within the dataset and has significant and positive weightings for Zn and Ga. Gallium behaves the same way as aluminium. A large part of the Eh–pH space (pH 6–10 for $a_{Ga} = 10^{-8}$) in the Ga–O–H system is occupied by the mineral söhngeite ($Ga(OH)_3$), which is a common compound in soils (Kabata-Pendias, 2011). In the Zn–O–H system, zinc is soluble as a divalent cation under circa-neutral to acidic conditions. Under circa-neutral to alkaline conditions, zinc may occur as the mineral zincite (ZnO) over a large part of the Eh–pH space (Brookins, 1988). F3 may represent the precipitation of Ga and Zn phases in a circa-neutral to mildly alkaline environment.

5.2. Ooid formation and growth

The pebbles from the Salento-type bauxite are remnants of a weathered and eroded bauxite deposit that likely formed during a middle Campanian emersion event, as stated above. The ooids from the Apulian karst bauxite formed in situ through a pedogenetic process, according to the mechanism of concretion formation in bauxites and ferricretes outlined by Tardy and Nahon (1985) and mineralogical variations of bauxites reflect palaeoclimate changes (e.g. Beauvais, 1999 and references therein). In this process, boehmite forms in bauxite-hosted ooids instead of Al-hematite, in the case that water activity is low (e.g. Mongelli et al., 2014 and references therein).

In the unsaturated zone in soil, capillary water activity at equilibrium is the ratio of the water partial pressure above the soil to the water partial pressure of the corresponding water-saturated air (Sposito, 1981). Boehmite stability is promoted during drainage and evaporation, as water is retained in pores of progressively smaller radius, the pressure is less than in the atmosphere, the water activity is less than one, and the aqueous silica concentration is also reduced as pore size decreases.

Dry conditions, and the associated reduction in soil water content, promote volumetric shrinking of the soil and intensive desiccation cracking (Kodikara and Costa, 2013). In turn, pervasive cracks lead to enhanced permeability (Stirling et al., 2013). Microcracks and fissures that form under such conditions can hinder the formation of spheroidal aggregates and reduce aggregate numbers. This explains the ooid circularity and aspect ratio data of the present study, and the low ooid/matrix ratio for the Salento-type pebbles relative to other Apulian karst bauxites (Mongelli et al., 2015).

Meakin (1991) showed that the aggregation of small particles to form larger structures is important in a wide range of natural processes, including mineral formation, and that these aggregates can be described in terms of fractal geometry. The growth of ooids within a bauxite matrix can be regarded as the growth of fractal aggregates, as the average D value for the Salento-type pebbles (1.59 ± 0.10) is close to values associated with experimental diffusion-limited aggregation models ($D = 1.62 \pm 0.4$) (Meakin, 1991 and references therein). This view is consistent with previous results demonstrating that the growth of sub-spherical concretions in bauxite is a chemical-transport-controlled phenomenon (e.g. Nahon, 1991; Tardy and Nahon, 1985) that can be modelled using a molecular diffusion pattern and assuming negligible fluid flow (Mongelli, 2002 and references therein). In recent years, diffusion-based models have been used to explain concretionary growth (e.g. Chan et al., 2004, 2007, 2012; Parry, 2011; Sefton-Nash and Catling, 2008).

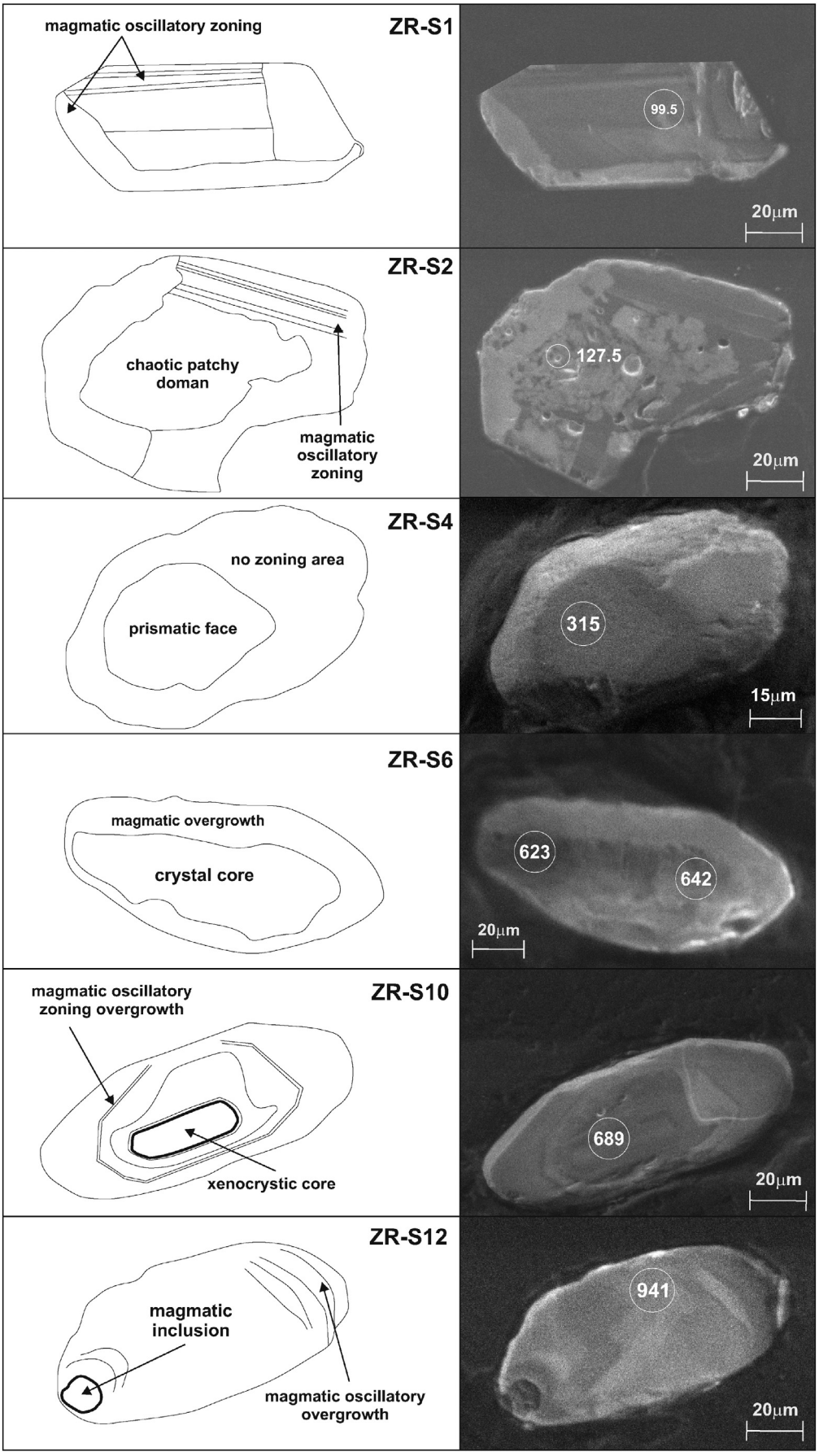

Fig. 6. Shape and zoning patterns of selected zircon grains from the Otranto bauxite. See text for further details.

In a stationary medium, the transport of *e* by molecular diffusion is proportional to the concentration gradient $\partial C/\partial x$, and the movement is described by Fick's first law (in one dimension):

$$J = -D(\partial C/\partial x)$$

where J is the mass moving across a unit area in unit time and the diffusion coefficient D is the constant of proportionality. The minus sign indicates the flux trends towards lower *e* concentrations. Assuming negligible fluid flow, the dissolution of pre-existing minerals, and simultaneous precipitation of a new mineral, growth occurs in a spheroidal geometry. During this process, a zone of depletion develops around each growing particle. According to Berner (1968), the time required to grow a spherical concretion with radius r_c is

$$t = r_c^2/2\nu D\Delta C$$

where ν is the molar volume of the precipitating mineral in the concretion and ΔC *is* the concentration gradient of source material between the surface of the concretion and a large distance from the concretion. When the host rock plays a role in sourcing the precipitate, the time required to grow the concretion is as follows (Wilkinson and Dampier, 1990):

$$t = r_c^2\left[1-\left(F_d/F_p\right)^{1/3}\right]/2\nu D_e\Delta C$$

where F_d is the volume fraction of the host rock occupied by source material (Al^{3+}) before concretion formation, and F_p is the volume fraction of the concretion occupied by precipitated material. D_e is the effective diffusion coefficient, as the diffusion coefficient in free water is related to the sediment properties through tortuosity. The diffusion coefficient for Al^{3+} in water at 25 °C and infinite dilution is $D = 0.559 \times 10^{-5}$ cm^2 s^{-1} (Steefel, 2007). However, when the diffusive flux is calculated according to Fick's law, and due to the linear relationship between tortuosity and porosity (Bear, 1972), the effective diffusion coefficient can be calculated as follows (Appelo and Postma, 1999):

$$D_e = D\phi$$

where ϕ is the porosity. Assuming the concretion formed in a kaolinite-rich soil, and using the porosity value of 0.27 determined for kaolinite clays (Diamond, 1970), the calculated effective diffusion coefficient for Al^{3+} is $D_e = 0.151 \times 10^{-5}$ cm^2 s^{-1}.

The solubility of boehmite is very low for the pH range associated with groundwater, and the Al^{3+} concentration at the surface of the concretion can be ignored. The concentration of Al^{3+} in soil water, for pH > 4, is particularly low (e.g. Fest et al., 2007), and we assume an Al^{3+} concentration of 0.5 mg/kg = 18.5×10^{-3} mol/m^3 away from the concretion. Since the ACP karst bauxite started as a kaolinite-rich soil (Mongelli et al., 2014), we can assume that F_d (i.e. the volume fraction of the host rock occupied by source material, Al^{3+}) is 0.4. The value for the volume fraction occupied by precipitated material (F_p), for a concretion entirely formed by boehmite, is assumed to be 0.45. The molar volume of boehmite is 19.507 cm^3/mol (Smyth and McCormick, 1995).

The calculated time required for the growth of an average boehmite concretion with a radius $r_p = 46.2 \pm 20.6$ is therefore ~150 ka. Based on the range of concretion radii within the standard deviation (r_p range = 25.6 ÷ 66.8 μm; std = ±20.6), the time required for growth is ~45 ÷ 310 ka. A maximum growth time of few ka for boehmite concretions is consistent with an intra-Campanian emersion event (74–76 Ma) related to a tectonic uplift (Morsilli and Rustichelli, 2004) and/or to a sea-level lowstand (Haq, 2014; Schlűter et al., 2008) during a warm climate phase, before the global cooling associated to the late Campanian-Maastrichtian interval (Dennis et al., 2013; Linnert et al., 2014), characterized by very low rainfall rates (Sellwood and Valdes, 2006; Scotese, 2014).

5.3. Provenance and palaeogeographic reconstruction

The formation of karst bauxite is associated with the fractionation of major, minor, and trace elements (e.g. Mongelli et al., 2014). Because the dissolution of carbonate bedrock is not considered a viable mechanism for ore formation, and because the Tethyan realm was strongly affected by tectonism during the Late Cretaceous (e.g. Handy et al., 2010; Schettino and Turco, 2011), it is difficult to assess the parental affinities of the karst bauxite. A number of palaeogeographic scenarios have been proposed to explain the provenance of other Late Cretaceous karst bauxite deposits in southern Italy. Based on zircon ages, the Matese Mts. bauxite deposit is potentially of volcanic wind-borne origin, sourced from the Dinaric and Carpatho-Balkan orogenic belts (Boni et al., 2012). Based on conservative elemental proxies, such as the europium anomaly (Mongelli et al., 2014), the autochthonous karst bauxite deposit of Spinazzola is a combination of windborne magmatic material from a distant source and dominant clastic material derived from the continental margin of North Africa to the south.

The Eu anomaly, which in sediments reflects the proportion of exposed crust in the source area(s) (e.g. Condie et al., 2001; Cullers, 2000; McLennan et al., 1993; Perri et al., 2013; Roser et al., 2002; Sinisi et al., 2014), has also proved to be an effective and reliable provenance proxy for bauxite (Mameli et al., 2007; Mongelli et al., 2014). Similar to the Eu/Eu* proxy, the Sm/Nd ratio reflects chemical differentiation, since only minor fractionation of Sm and Nd occurs during intense tropical weathering (Viers and Wasserburg, 2004). The Sm/Nd ratio has been used to determine parental affinities for Tethyan karst bauxite (Mongelli et al., 2014). In the Eu/Eu* vs Sm/Nd binary diagram (Fig. 8), the pebbles of the allochthonous Salento-type karst bauxite plot close to a mixing curve with cratonic sandstone and andesite as end-members. The Late Cretaceous autochthonous Apulian karst bauxites plot in a similar area, thus indicating that the two bauxite types have a common provenance.

If the presence of andesite as an end-member for the mixing curve supports the suggestion that volcanics may act as parental material, the other end-member reflects siliciclastic sediments and suggests that the ACP was linked to a continental margin during the Cretaceous. It has to be stressed that siliciclastic clay-rich beds occur in the Apulian carbonate sequences as documented by Iannone and Laviano (1980) and Laviano et al. (1998). Although windborne transport cannot be excluded a transport mechanism other than the eolian one may also justify the presence of clay-rich beds. The contour currents are an example of transport vehicles alternative to the wind and fluvial system. Evidences of currently active contour-transportation are widely documented worldwide (Stow et al., 1998) as for example along the Antarctica continent where wide contourite deposits occur. The contour currents develop mostly along continental margins and are able to carrying significant amounts of sediment away from the source area (Stow et al., 1998; Weaver et al., 2000; Rodriguez and Anderson, 2004). As a consequence, in the proposed palaeogeographic realm we don't need to justify the siliciclastic supply to the ACP exclusively through wind and/or a fluvial transport system. Furthermore, the statement of contour drift along the ACP close to the cratonic area has important implications on palaeotectonics and palaeogeography of the study area supporting the scenario of a physical linkage between the African Craton and the Apulian Platform. Further evidence for this interpretation is provided by the widespread and numerous dinosaur footprints in the ACP since the Lower Cretaceous age (Zarcone et al., 2010 and references therein). These footprints are proposed to record the periodic migration from a southern continental landmass (Bosellini, 2002). In this scenario, the ACP was part of a larger carbonate platform (Nicosia et al., 2007; Petti et al., 2008; Zarcone et al., 2010), where fluctuating

Table 4
Results of the LA-ICP-MS U–Pb analysis of zircon grains from the Otranto bauxite.

Sample	Isotopic ratios						Age estimates (Ma)						% U–Pb disc	Concordant age	
	$^{207}Pb/^{206}Pb$	±1σ	$^{206}Pb/^{238}U$	±1σ	$^{207}Pb/^{235}U$	±1σ	$^{207}Pb/^{206}Pb$	±1σ	$^{206}Pb/^{238}U$	±1σ	$^{207}Pb/^{235}U$	±1σ		Age (Ma)	2σ
ZrS1	0.04761	0.00164	0.01555	0.00034	0.10194	0.00290	80	3	99	2	99	3	−0.9	99	4.3
ZrS2	0.04913	0.00227	0.01555	0.00036	0.10483	0.00437	154	7	99	2	101	4	1.7	99.5	4.6
ZrS3	0.04792	0.00863	0.01759	0.00050	0.11593	0.02064	95	17	112	3	111	20	−0.9	112.4	6.4
ZrS4	0.04910	0.00857	0.01998	0.00061	0.13443	0.02316	153	27	128	4	128	22	0.4	127.5	7.8
ZrS5	0.05294	0.00219	0.05001	0.00118	0.36358	0.01391	326	13	315	7	315	12	0.1	315	14
ZrS6	0.06097	0.00252	0.10131	0.00232	0.85343	0.03282	638	26	622	14	627	24	0.7	623	27
ZrS6b	0.06143	0.00224	0.10463	0.00239	0.88708	0.02951	654	24	641	15	645	21	0.5	642	27
ZrS7	0.06072	0.00197	0.10163	0.00240	0.85433	0.02504	629	20	624	15	627	18	0.5	626	26
ZrS8	0.06160	0.00210	0.10460	0.00243	0.88593	0.02721	660	22	641	15	644	20	0.4	643	27
ZrS9	0.06201	0.00248	0.10805	0.00259	0.92251	0.03439	674	27	661	16	664	25	0.3	662	29
ZrS10	0.06234	0.00152	0.11419	0.00258	0.97720	0.01978	686	17	697	16	692	14	−0.7	689	18
ZrS11	0.06763	0.00181	0.14602	0.00331	1.36685	0.03127	857	23	879	20	875	20	−0.4	866	11
ZrS12	0.07149	0.00498	0.15714	0.00472	1.53157	0.10299	971	68	941	28	943	63	0.2	941	51

Cretaceous sea levels periodically exposed large parts of the inner platform facies.

Zircon age dating may help to verify this picture. Despite the paucity of zircon grains, they yield valuable information on their age and origin. The grains collected from the pebbles of the ACP Salento-type karst bauxite record several concordant age populations. The youngest cluster, Early Cretaceous in age (99 ÷ 127.5 Ma), suggests that windborne particles from Early Cretaceous Carpatho-Balkan volcanics, (e.g. Csontos and Vörös, 2004; Harangi, 1994; Nédli and Tóth, 2002) were afterward transported to low latitudes by prevailing easterlies (Hay, 2008) providing material for further bauxitization during Campanian age. The single zircon with an age of 315 Ma likely represents a xenocryst that was incorporated into Cretaceous magmas and erupted together with the youngest zircon population.

The largest cluster (623 ÷ 689 Ma; n = 6) is of Neoproterozoic age, predominately Cryogenian. The 900–540 Ma Pan-African orogenic cycle ended with the assembly of Gondwana in the late Neoproterozoic and was followed by continental-scale uplift and erosion that in turn led to the deposition of thick siliciclastic sequences on the margins of the supercontinent, today covering large parts of northern Africa (e.g. Avigad et al., 2003 and references therein). These Cambrian–Ordovician siliciclastic sequences are the most widespread detrital sequences ever deposited on continental crust (Burke et al., 2003) and formed as a consequence of widespread chemical weathering of the Pan-African continental basement (Avigad et al., 2005). The Cambrian–Ordovician sandstones, from Morocco in the east to Israel and Jordan in the west, contain a large Neoproterozoic zircon population with many crystals of Cryogenian age (e.g. Abati et al., 2010, 2012; Altumi et al., 2013; Avigad et al., 2003, 2005, 2012; Meinhold et al., 2011, 2013, 2014). Meinhold et al. (2011) reported that Neoproterozoic zircons also occur in Silurian, Devonian, Carboniferous, and Mesozoic sandstones from the Saharan Metacraton. These sandstones also contain varying amounts of ~1.0 Ga detrital zircons. The two zircons in our study with ages of 866 and 941 Ma are likely younger representatives (Tonian age) of the ~1.0 Ga cluster. The Neoproterozoic age for most of the zircons from the pebbles of the Salento-type bauxite therefore indicates their provenance is from North African cratonic sandstones. This inference suggests that the ACP was a spur of the north-western African platform, where fluctuating Cretaceous sea levels periodically exposed large parts of the shallow-water carbonate platforms (Nicosia et al., 2007; Petti et al., 2008; Zarcone et al., 2010). Although between ~20°N and 30°N the climate during the Late Cretaceous was generally dry, sporadic rain events (Scotese, 2014) could have supplied clastic material to the carbonate platform (Fig. 9), further accumulated in karst cavities and become bauxitised.

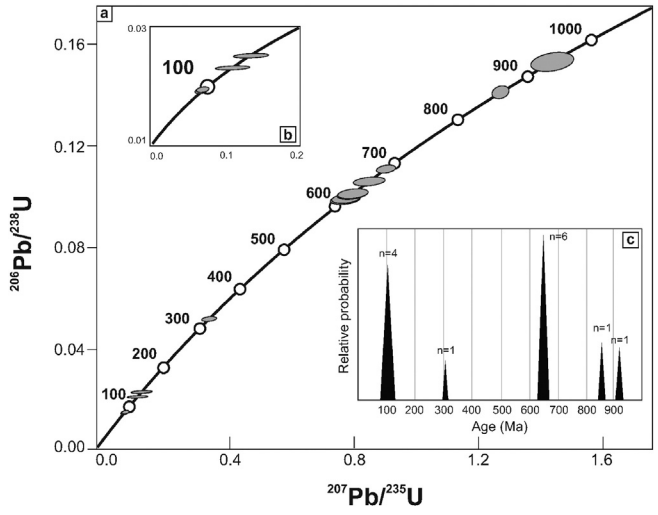

Fig. 7. a) Concordia diagram showing LA-ICP-MS U-Pb geochronologic data of zircons from the Otranto bauxite deposit. b) Inset displaying the younger population of zircon grains. c) Inset giving the relative probability of ages for data shown in (a).

6. Conclusions

Pebbles from a Salento-type allochthnous bauxite deposit in the ACP and originally derived from a pristine Campanian bauxite confirm the capability of bauxite to concentrate many elements defined as critical by the European Union report on critical raw materials (2014). Some of these elements (e.g. Sc, Co, Ga and especially Cr) are enriched.

Table 5
R-mode factor analysis results after Varimax rotation

	Factor 1	Factor 2	Factor 3	Communalities
TiO_2	−0.78			0.97
Al_2O_3	−0.68			0.95
Fe_2O_3	0.72			0.98
Sc	0.83			0.99
V	0.92			0.95
Cr		−0.69		0.99
Co		0.85		0.99
Ni		0.89		0.99
Cu				0.91
Zn			0.73	0.99
Ga			0.90	0.99
Zr				0.99
Nb	−0.77			0.99
REEs	0.96			0.99
Hf				0.96
Pb	0.93			0.99
Th	0.87			0.99
Var %	52.6	22.8	13.2	

Note: Numbers are weights of the variables in the extracted factors. Variables having weight less than 0.65 are omitted.

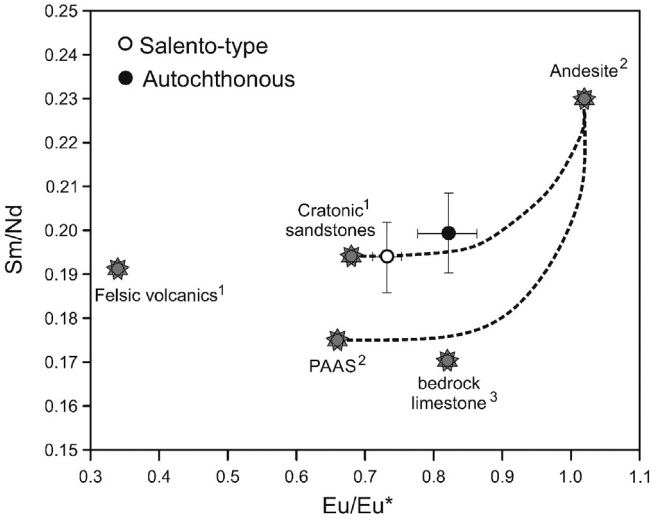

Fig. 8. Eu/Eu* vs Sm/Nd binary plot showing mixing lines between average standard lithologies. Circles are bauxite from the Otranto site. 1: Condie (1993); 2: Taylor and McLennan (1985); 3: Mongelli et al. (2014).

Other critical elements such as the REEs, with the exception of La, are moderately depleted when compared with the UCC and assuming Nb is immobile. R-mode factor analysis suggests that most of the variance in our chemical data (which includes values for TiO_2, Al_2O_3, Fe_2O_3, critical elements, transition metals and HFSE) is explained by a factor with significant weightings for TiO_2, Al_2O_3, Fe_2O_3, Sc, V, Nb, REEs, Pb and Th. Among the critical elements, Sc is controlled by iron oxy-hydroxides, whereas Nb is linked with TiO_2, as would be expected. The link between Fe_2O_3 and the REEs, Th, and Pb is interpreted to indicate the accumulation of tiny weathering-resistant crystals during a wetter stage.

The pebbles also record information on the palaeoclimate and palaeogeography of the Late Cretaceous Peri-Tethyan realm. The texture of the pebbles is typical for Apulian karst bauxites and consists of sub-spheroidal ooids dispersed in a fine-grained matrix. The ooids are composed of boehmite and locally have a thin rim of Al-hematite. Boehmite forms under conditions of low water activity, and the dry climate resulted in pervasive microcracks and fissures in the fine-grained parent material, hindering ooid formation. This explains the low ooid/matrix ratio compared with other Apulian karst bauxites. The growth of the ooids can be described in terms of fractal geometry, and the average value of the fractal dimension of the ooids in the pebbles is close to the value for diffusion-limited aggregation models. Thus, in the case of growth of sub-spheroidal concretions in bauxite via chemical-transport-controlled processes, the growth can be modelled using a molecular diffusion pattern and assuming negligible fluid flow, based on Fick's first law. The calculated time required for growth of the boehmite concretions is ~45 ÷ 310 ka. This finding is consistent with both an intra-Campanian emersion event (74–76 Ma), a sea

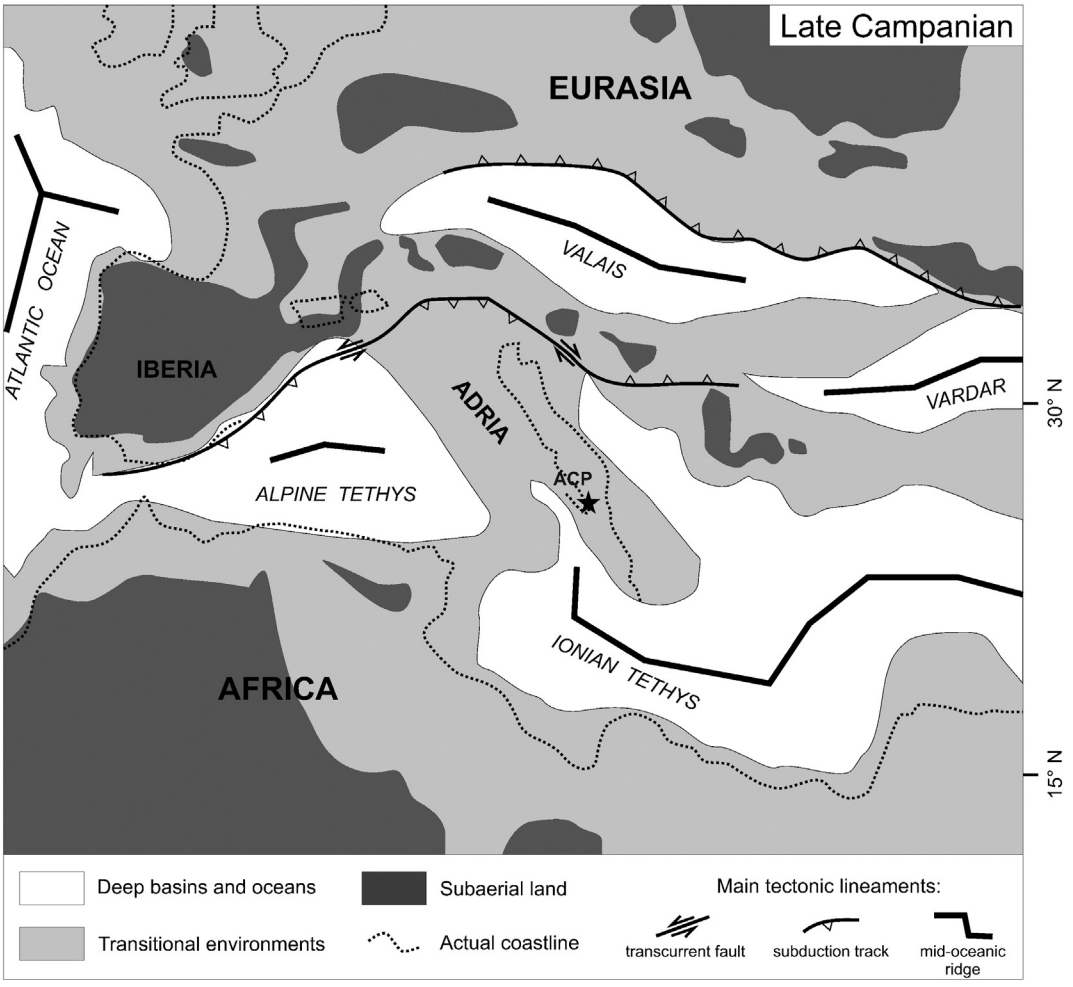

Fig. 9. Paleogeographic sketch map of the Mediterranean area during Late Cretaceous. Plate reconstruction and paleolatitude are after Scotese (2014). The star is for location of the Otranto bauxite deposit on the ACP microplate.

level lowstand that occurred during a dry and warm climatic stage, and with the 1 ÷ 5 Ma estimated hiatus time necessary to form karst bauxite deposits (Bárdossy, 1982). Since most of the karst bauxites worldwide have an ooidic texture (Bárdossy, 1982), evaluation of the composition of concretions and the time required for their growth represents a powerful tool in reconstructing the palaeonvironment.

The rare zircon grains in the bauxite furnish useful information on palaeogeography, as the analysed grains provide enough data to constrain the age and origins of the zircons. The grains collected from the pebbles of the ACP Salento-type karst bauxite define several concordant age populations. The youngest cluster, Early Cretaceous in age (99 ÷ 127.5 Ma), suggests that windborne particles from Cretaceous volcanics, possibly originating in the Carpatho-Balkan orogenic belts, accumulated on the ACP and provided material for further bauxitisation. The largest cluster (623 ÷ 689 Ma) is of Neoproterozoic age, predominately from the Cryogenian. The 900–540 Ma Pan-African orogenic cycle was followed by continental-scale uplift and erosion, leading to the deposition of thick Cambrian–Ordovician siliciclastic sequences that represent the most widespread detrital sequence ever deposited on continental crust and that now cover large parts of North Africa. These Cambrian–Ordovician sandstones contain a large population of Neoproterozoic zircons of Cryogenian age. Neoproterozoic zircons also occur in the youngest (Silurian–Mesozoic) sandstones of the Saharan Metacraton. These sandstones also contain 1.0 Ga detrital zircons, suggesting the oldest zircons found in the Salento-type bauxite pebbles (866 Ma and 941 Ma in age) are younger representatives of the zircon cluster present in this sandstone unit. These zircon dates suggest the source material for the Salento-type bauxite pebbles was a combination of eastern windborne volcanics and clastic material, transported by contour currents, derived from a continental margin (North Africa) to the south. This result concurs with the Eu/Eu* vs. Sm/Nd binary diagram, on which bauxite pebbles fall close to a mixing curve with cratonic sandstone and andesite as end-members. This finding is similar to that observed for Late Cretaceous autochthonous Apulian karst bauxites, suggesting a similar provenance in both cases. As our results indicate that material was sourced from the North African continental margin, we suggest that in the Late Cretaceous a continental bridge separated oceanic domains of the Peri-Tethyan domain (Fig. 9) also according to the widespread and numerous dinosaur footprints in the ACP since the lower Cretaceous age recording periodic migration from a southern continental landmass.

Acknowledgements

The research was supported by a G. Mongelli grant (RIL 2013). The authors are indebted to M. Boni for the valuable work during sampling and for the fruitful discussions on bauxite origin. Many thanks to A. Laurita, University of Basilicata, for his support during the ESEM-EDS analysis and to prof. W. Cavazza, Department of Biological, Geological and Environmental Sciences of the University of Bologna 'Alma Mater', for the zircon grain separation facilities. The authors are also very grateful to the Editor-in-Chief (Prof. Franco Pirajno) and the anonymous reviewer for their helpful suggestions that improved the manuscript.

References

Abati, J., Aghzer, A.M., Gerdes, A., Ennih, N., 2010. Detrital zircon ages of Neoproterozoic sequences of the Moroccan Anti-Atlas belt. Precambrian Res. 181, 115–128.
Abati, J., Aghzer, A.M., Gerdes, A., Ennih, N., 2012. Precambrian Res. 212-213, 263–274.
Abedini, A., Calagari, A.A., 2014. REE geochemical characteristics of titanium-rich bauxites: the Permian Kanigorgeh horizon, NW Iran. Turk. J. Earth Sci. 23, 513–532.
Altumi, M.M., Elicki, O., Linnemann, U., Hofmann, M., Sagawe, A., Gartner, A., 2013. U-Pb LA-ICP-MS detrital zircon ages from the Cambrian of Al Qarqaf Arch, central-western Libya: Provenance of the West Gondwanan sand sea at the dawn of the early Palaeozoic. J. Afr. Earth Sci. 79, 74–97.
Appelo, C.A.J., Postma, D., 1999. Variable dispersivity in a column experiment containing MnO_2 and FeOOH coated sand. J. Contam. Hydrol. 40, 95–106.
Avigad, D., Kolodner, K., McWilliams, M., Persing, H., Weissbrod, T., 2003. Origin of northern Gondwana Cambrian sandstone revealed by detrital zircon SHRIMP dating. Geology 31, 227–230.
Avigad, D., Sandler, A., Kolodner, K., Stern, R.J., McWilliams, M., Miller, N., Beyth, M., 2005. Mass-production of Cambro–Ordovician quartz-rich sandstone as a consequence of chemical weathering of Pan-African terranes. Environmental implications. Earth Planet. Sci. Lett. 240, 818–826.
Avigad, D., Gerdes, A., Morag, N., Bechstädt, T., 2012. Coupled U–Pb–Hf of detrital zircons of Cambrian sandstones from Morocco and Sardinia: implications for provenance and Precambrian crustal evolution of North Africa. Gondwana Res. 21, 690–703.
Bárdossy, G., 1982. Karst bauxites. Bauxite deposits on carbonate rocks. Developments in Economic Geology vol. 14. Elsevier, Amsterdam.
Bear, J., 1972. Dynamic of fluids in porous media. American Elsevier, New York.
Beauvais, A., 1999. Geochemical balance of laterization processes and climatic signatures in weathering profiles overlain by ferricretes in Central Africa. Geochim. Cosmochim. Acta 63, 3939–3957.
Berner, R.A., 1968. Calcium carbonate concretions formed by the decomposition of organic matter. Science 159, 195–197.
Bernoulli, D., 2001. Mesozoic-Tertiary carbonate platforms, slopes and basins of the external Apennines and Sicily. In: Vai, G.B., Martini, I.P. (Eds.), Anatomy of an Orogen: the Apennines and adjacent Mediterranean basins. Kluwer Academic Publishers, Great Britain.
Bogatyrev, B.A., Zhukov, V.V., 2009. Bauxite provinces of the world. Geol. Ore Deposits 51, 339–355.
Boni, M., Reddy, S.M., Mondillo, N., Balassone, G., Taylor, R., 2012. A distant magmatic source for Cretaceous karst bauxites of southern Apennines (Italy) revealed through SHRIMP zircon age dating. Terra Nova 24, 326–332.
Boni, M., Rollinson, G., Mondillo, N., Balassone, G., Santoro, L., 2013. Quantitative mineralogical characterization of karst bauxite deposits in the Southern Apennines, Italy. Econ. Geol. 108, 813–833.
Bosellini, A., 2002. Dinosaurs "re-write" the geodynamics of the eastern Mediterranean and the paleogeography of the Apulia Platform. Earth Sci. Rev. 59, 211–234.
Bosellini, A., 2004. The western passive margin of Adria and its carbonate platforms: Special Volume of the Italian Geological Society for the IGC 32. pp. 79–92.
Brookins, D.G., 1988. Eh-pH diagrams for geochemistry. Springer-Verlag, New York.
Burke, K., McGregor, D.S., Cameron, N.R., 2003. African Petroleum Systems: four tectonic Aces in the past 600 million years. Geol. Soc. Lond. Spec. Publ. 207, 21–60.
Chan, M.A., Beitler, B., Parry, W.T., Ormö, J., Komatsu, G., 2004. A possible terrestrial analogue for hematite concretions on Mars. Nature 429, 731–734.
Chan, M.A., Ormö, J., Park, A.J., Stich, M., Souza-Egipsy, V., Komatsu, G., 2007. Models of iron oxide concretion formation: field. Numer. Lab. Comparisons Geofluids 7, 356–368.
Chan, M.A., Potter, S.L., Bowen, B.B., Petersen, E.U., Parry, W.T., Bowman, J.R., Barge, L., Seiler, W., 2012. Characteristics of terrestrial ferric oxide concretions and implications for Mars. In: Grotzinger, J., Milliken, R. (Eds.), Sedimentary Geology of Mars. SEPM Special Publication 102, pp. 253–270.
Channell, J.E.T., 1996. Palaeomagnetism and palaeogeography of Adria. In: Morris, A., Tarling, D.H. (Eds.), Palaeomagnetism and Tectonics of the Mediterranean Region: Geological Society of London. Special Publication 105, pp. 119–135.
Ciaranfi, N., Pieri, P., Ricchetti, G., 1992. Note alla Carta Geologica delle Murge e del Salento (puglia Centro-Meridionale). Mem. Soc. Geol. Ital. 41, 449–460.
Cloething, S., Haq, B.U., 2015. Inherited landscapes and sea level change. Science 347, 393–404. http://dx.doi.org/10.1126/science.1258375.
Condie, K.C., 1993. Chemical composition and evolution of the upper continental crust: contrasting results from surface samples and shales. Chem. Geol. 104, 1–37.
Condie, K.C., Marais, D.J.D., Abbott, D., 2001. Precambrian superplumes and supercontinents: a record in black shales, carbon isotopes, and paleoclimates. Precambrian Res. 106, 239–260.
Csontos, L., Vörös, A., 2004. Mesozoic plate tectonic reconstruction of the Carpathian region. Palaeogeogr. Palaeoclimatol. Palaeoecol. 210, 1–56.
Cullers, R.L., 2000. The geochemistry of shales, siltstones and sandstones of Pennsylvanian–Permian age, Colorado, USA: implications for provenance and metamorphic studies. Lithos 51, 181–203.
Davis, J.C., 1986. Statistics and Data Analysis in Geology. John Wiley & Sons, New York.
Delvigne, J., 1998. Atlas of micromorphology of mineral alteration and weathering. The Canadian Mineralogist, Special Publication No. 3, Ottawa.
Dennis, K.J., Cochran, J.K., Landman, N.H., Schrag, D.P., 2013. The climate of the Late Cretaceous: new insights from the application of the carbonate clumped isotope thermometer to Western Interior Seaway macrofossil. Earth Planet. Sci. Lett. 362, 51–65.
Dercourt, J., Gaetani, M., Vrielynck, B., Barriere, E., Biju-Duval, B., Brunet, M.F., Cadet, J.P., Crasquin, S., Sandulescu, M.E., 2000. Atlas Peri-Tethys, Palaeogeographical Maps (CCGM/CGMW, 269 pp., 24 maps).
Dewey, J.F., Helman, M.L., Turco, E., Hutton, D.H.W., Knott, S.D., 1989. Kinematics of the western Mediterranean. In: Coward, D., Dietrich, D., Park, R.G. (Eds.), Alpine Tectonics. Geological Society of London, Special Publication 45, pp. 265–283.
Diamond, S., 1970. Pore size distributions in clays. Clay Clay Miner. 18, 7–23.
Esu, D., Girotti, O., 2010. The late Oligocene molluscan fauna from Otranto (Apulia, Southern Italy): an example of alternating freshwater, lagoonal and emerged environments. Palaeontology 53, 137–174.
Evensen, N.M., Hamilton, P.J., Onions, R.K., 1978. Rare-Earth abundances in chondritic meteorites. Geochim. Cosmochim. Acta 42, 1199–1212.
Fest, E.P.M.J., Temminghoff, E.J.M., Griffioen, J., Van der Grift, B., Van riemsdijk, W.H., 2007. Groundwater chemistry of Al under Dutch sandy soils: effects of land use and depth. Appl. Geochem. 22, 1427–1438.
Finetti, I.R., 2005. Geodynamic evolution of the Mediterranean region from the Permo-Triassic Ionian opening to the present, constrained by new lithospheric

CROP seismic data. In: Finetti, I. (Ed.), CROP Project: Deep seismic exploration of the Central Mediterranean and ItalyAtlases in Geoscience 1. Elsevier, pp. 767–776.
Gaillardet, J., Viers, J., Dupre, B., 2003. Trace elements in river waters. In: Drever, J.I. (Ed.), Treatise of Geochemistry. Elsevier-Pergamon, Oxford.
Gow, N.N., Lozej, G.P., 1993. Bauxite. Geosci. Can. 20, 9–16.
Handy, M.R., Schmid, S.M., Bousquet, R., Bernoulli, D., 2010. Reconciling plate-tectonic reconstructions of Alpine Tethys with the geological–geophysical record of spreading and subduction in the Alps. Earth Sci. Rev. 102, 121–158.
Hanilçi, N., 2013. Geological and geochemical evolution of the Bolkardağı bauxite deposits, Karaman, Turkey: transformation from shale to bauxite. J. Geochem. Explor. 133, 118–137.
Haq, B.U., 2014. Cretaceous eustasy revisited. Glob. Planet. Chang. 113, 44–58.
Harangi, S., 1994. Geochemistry and petrogenesis of the Early Cretaceous continental rift-type volcanic rocks of the Mecsek Mountains, South Hungary. Lithos 33, 303–321.
Hardenbol, J., Vail, P.R., 1998. Upper Cretaceous sequence chronostratigraphy. In: Graciansky de, P.-C., Hardenbol, J., Vail, P.R. (Eds.), Mesozoic and Cenozoic Sequence Stratigraphy of European basins. Society of Economic Paleontologists and Mineralogists, Special Publication 60, pp. 774–775.
Hay, W.W., 2008. Evolving ideas about the Cretaceous climate and ocean. Cretac. Res. 29, 725–753.
Herrington, R., 2013. Road map to mineral supply. Nat. Geosci. 6, 892–894.
Horn, I., Rudnik, R.L., McDonough, W.F., 2000. Precise elemental and isotope ratio determination by simultaneous solution nebulization and laser ablation-ICP-MS: application to U–Pb geochronology. Chem. Geol. 164, 281–301.
Horstwood, M.S.A., Foster, G.L., Parrish, R.R., Noble, S.R., Nowell, G.M., 2003. Common-Pb corrected in situ U–Pb accessory mineral geochronology by LA–MC–ICP–MS. J. Anal. At. Spectrom. 18, 837–846.
Iannone, A., Laviano, A., 1980. Studio stratigrafico e paleoambientale di una successione Cenomaniano-Turoniana (Calcare di Bari) affiorante presso Ruvo di Puglia. Geol. Romana 19, 209–230.
Jarvis, I., Mabrouk, A., Moody, R.T.J., Cabrera de, S., 2002. Late Cretaceous (Campanian) carbon isotope events, sea-level change and correlation of the Tethyan and Boreal realms. Palaeogeogr. Palaeoclimatol. Palaeoecol. 188, 215–248.
Kabata-Pendias, A., 2011. Trace elements in soils and plants. fourth ed. CRC Press, Boca Raton.
Karadağ, M.M., Küpeli, S., Arýk, F., Ayhan, A., Zedef, V., Döyen, A., 2009. Rare earth element (REE) geochemistry and genetic implications of the Mortaş bauxite deposit (Seydişehir/Konya — Southern Turkey). Chem. Erde-Geochem. 69, 143–159.
Ketchum, J.W.F., Jackson, S.E., Culshaw, N.G., Barr, S.M., 2001. Depositional and tectonic setting of the Paleo-proterozoic Lower Aillik Group, Makkovik Province, Canada: evolution of a passive margin-foredeep sequence based on petrochemistry and U–Pb (TIMS and LAM-ICP-MS) geochronology. Precambrian Res. 105, 331–356.
Kodikara, J., Costa, S., 2013. Desiccation cracking in clayey soils: mechanism and modelling. In: Laloui, L., Ferrari, A. (Eds.), Multiphysical testing of soils and shales. Springer-Verlag, pp. 21–32.
Laviano, A., Gallo Maresca, M., Tropeano, M., 1998. Stratigraphic organization of rudist biogenic beds in the upper Cenomanian successions of the western Murge (Apulia, southern Italy). Geobios 31, 159–168.
Ling, K.Y., Zhua, X.Q., Tanga, H.S., Wanga, Z.G., Yanc, H.W., Hana, T., Chend, W.Y., 2015. Mineralogical characteristics of the karstic bauxite deposits in the Xiuwen ore belt, Central Guizhou Province, Southwest China. Ore Geol. Rev. 65, 84–96.
Linnert, C., Robinson, S.A., Lees, J.A., Bown, P.R., Perez-Rodrıguez, I., Petrizzo, M.R., Falzoni, F., Littler, K., Arz, J.A., Russell, E.E., 2014. Evidence for global cooling in the Late Cretaceous. Nat. Commun. 5, 4194–5194.
Mameli, P., Mongelli, G., Oggiano, G., Dinelli, E., 2007. Geological, geochemical and mineralogical features of some bauxite deposits from Nurra (Western Sardinia, Italy): insights on conditions of formation and parental affinity. Int. J. Earth Sci. 96, 887–902.
Margiotta, S., Mongelli, G., Summa, V., Paternoster, M., Fiore, S., 2012. Trace element distribution and Cr(VI) speciation in Ca–HCO_3 and Mg–HCO_3 spring waters from the northern sector of the Pollino massif, southern Italy. J. Geochem. Explor. 115, 1–12.
McLennan, S.M., Hemming, S., McDaniel, D.K., Hanson, G.N., 1993. Geochemical approaches to sedimentation, provenance and tectonics. In: Johnsson, M.J., Basu, A. (Eds.), Processes Controlling the Composition of Clastic Sediments. Geological Society of America, Special Papers 285, pp. 21–40.
Meakin, P., 1991. Fractals aggregates in geophysics. Rev. Geophys. 29, 317–354.
Meinhold, G., Morton, A.C., Fanning, C.M., Frei, D., Howard, J.P., Phillips, R.J., Strogen, D., Whitham, A.G., 2011. Evidence from detrital zircons for recycling of Mesoproterozoic and Neoproterozoic crust recorded in Paleozoic and Mesozoic sandstones of southern Libya. Earth Planet. Sci. Lett. 312, 164–175.
Meinhold, G., Howard, J.P., Strogen, D., Kaye, M.D., Abutarruma, Y., Elgadry, M., Thusu, B., Whitham, A.G., 2013. Hydrocarbon source rock potential and elemental composition of lower Silurian subsurface shales of the eastern Murzuq Basin, southern Libya. Mar. Pet. Geol. 48, 224–246.
Meinhold, G., Morton, A.C., Fanning, C.M., Howard, J.P., Phillips, R.J., Strogen, D., Whitham, A.G., 2014. Insights into crust formation and recycling in North Africa from combined detrital zircon U-Pb, Lu-Hf and O isotope data from Devonian sandstone of southern Libya. In: Scott, R.A., Smyth, H.R., Morton, A.C., Richardson, N. (Eds.), Sediment Provenance Studies in Hydrocarbon Exploration and Production. Geological Society, London, Special Publications 386, pp. 281–292.
Meyer, F.M., 2004. Availability of bauxite reserves. Nat. Resour. Res. 13, 161–172.
Mindszenty, A., D'Argenio, B., Aiello, G., 1995. Lithospheric bulges at regional unconformities. The case of Mesozoic-Tertiary in Apulia. Tectonophysics 252, 137–161.
Mongelli, G., 1997. Ce-anomalies in the textural components of Upper Cretaceous karst bauxites from the Apulian Carbonate Platform (southern Italy). Chem. Geol. 140, 69–79.
Mongelli, G., 2002. Growth of hematite and boehmite in concretions from ancient karst bauxite: clue for past climate. Catena 50, 43–51.
Mongelli, G., Acquafredda, P., 1999. Ferruginous concretions in a Late Cretaceous karst bauxite: composition and conditions of formation. Chem. Geol. 158, 315–320.
Mongelli, G., Boni, M., Buccione, R., Sinisi, R., 2014. Geochemistry of the Apulian karst bauxites (southern Italy): chemical fractionation and parental affinities. Ore Geol. Rev. 63, 9–21.
Mongelli, G., Buccione, R., Sinisi, R., 2015. Genesis of autochthonous and allochthonous Apulian karst bauxites (Southern Italy): climate constraints. Sediment. Geol. 325, 168–176.
Morsilli, M., Rustichelli, G., 2004. Event stratigraphy and correlation between two sectors of the Apulia Carbonate Platforms during the Cretaceous (Italy). 32nd IGC, Florence.
Nahon, D., 1991. Introduction to the Petrology of Soils and Chemical Weathering. Wiley, New York.
Nédli, Z., Tóth, T.M., 2002. Subduction-related volcanism in the SW Tisia and its geodynamic consequences. Proceedings of XVII Congress of Carpathian-Balkan Geological Association. Bratislava, September 1-4. Geologica Carpathica vol. 53.
Nesbitt, H.W., 1979. Mobility and fractionation of rare earth elements during weathering of a granodiorite. Nature 279, 206–210.
Nicosia, U., Petti, F.M., Perugini, G., D'Orazi, Porchetti S., Sacchi, E., Conti, M.A., Mariotti, N., Zarattini, A., 2007. Dinosaur tracks as paleogeographic constraints: new scenarios for the Cretaceous geography of the periadriatic region. Ichnos 14, 69–90.
Parry, W.T., 2011. Composition, nucleation, and growth of iron oxide concretions in the Jurassic Navajo Sandstone, Utah. Sediment. Geol. 233, 53–68.
Peh, Z., Kovačević Galović, E., 2014. Geochemistry of Istrian Lower Palaeogene bauxites: is it relevant to the extent of subaerial exposure during Cretaceous times? Ore Geol. Rev. 63, 296–306.
Perri, F., Critelli, S., Martìn-Algarra, A., Martìn-Martìn, M., Perrone, V., Mongelli, G., Zattin, M., 2013. Triassic redbeds in the Malaguide Complex (Betic Cordillera — Spain): petrography, geochemistry, and geodynamic implications. Earth Sci. Rev. 117, 1–28.
Petti, F.M., D'orazi, Porchetti S., Conti, M.A., Nicosia, U., Perugini, G., Sacchi, E., 2008. Theropod and sauropod footprints in the Early Cretaceous (Aptian) Apenninic Carbonate Platform (Esperia, Lazio, Central Italy): a further constraint on the palaeogeography of the Central-Mediterranean area. Stud. Trent. Sci. Nat. Acta Geol. 83, 323–334.
Ricchetti, G., Ciaranfi, N., Luperto Sinni, E., Mongelli, F., Pieri, P., 1992. Geodinamica ed evoluzione sedimentaria e tettonica dell'avanpaese apulo. Mem. Soc. Geol. Ital. 41, 57–82.
Rodriguez, A.B., Anderson, J.B., 2004. Contourite origin for shelf and upper slope sand sheet, offshore Antarctica. Sedimentology 51, 699–711.
Roser, B.P., Coombs, D.S., Korsch, R.J., Campbell, J.D., 2002. Whole-rock geochemical variations and evolution of the arc-derived Murihiku Terrane, New Zealand. Geol. Mag. 139, 665–685.
Schettino, A., Turco, E., 2011. Tectonic history of the western Tethys since the Late Triassic. Geol. Soc. Am. Bull. 123, 89–105.
Schlűter, M., Steuber, T., Parente, M., 2008. Chronostratigraphy of Campanian-Maastrichtian platform carbonates and rudist associations of Salento (Apulia, Italy). Cretac. Res. 29, 100–114.
Scotese, C.R., 2014. Atlas of Phanerozoic Rainfall Maps (Mollweide Projection). *PALEOMAP Project* PaleoAtlas for ArcGIS vol. 1-6. PALEOMAP Project, Evanston, IL.
Sefton-Nash, E., Catling, D.C., 2008. Hematitic concretions at Meridiani Planum, Mars: their growth timescale and possible relationship with iron sulfates. Earth Planet. Sci. Lett. 269, 366–376.
Sellwood, B.W., Valdes, P.J., 2006. Mesozoic climates: general circulation models and the rock record. Sediment. Geol. 190, 269–287.
Sinisi, R., Mongelli, G., Mameli, P., Oggiano, G., 2014. Did the Variscan relief influence the Permian climate of Mesoeurope? Insights from geochemical and mineralogical proxies from Sardinia (Italy). Palaeogeogr. Palaeoclimatol. Palaeoecol. 396, 132–154.
Smith, K.S., 1999. Metal sorption on mineral surfaces: an overview with examples relating to mineral deposits. In: Plumlee, G.S., Logsdon, M.J. (Eds.), The Environmental Geochemistry of Mineral Deposits, Part A: Processes, Techniques, and Health IssuesRev. Econ. Geol. vol. 6. Society of Economic Geologists, Inc., Littleton, Colorado, pp. 161–182.
Smyth, J.R., McCormick, T.C., 1995. Crystallographic data for minerals. In: Ahrens, T.J. (Ed.), Mineral Physics and Crystallography: A Handbook of Physical Constants. AGU, Washington DC, pp. 1–17.
Sposito, G., 1981. The Thermodynamics of Soil Solutions. Claren- don Press, Oxford.
Stampfli, G.M., 2000. Tethyan Oceans. In: Bozkurt, E., Winchester, J.A., Piper, J.D.A. (Eds.), Tectonics and Magmatism in Turkey and the Surrounding AreaGeol. Soc. Lond., Spec. Publ. 173, 1–23.
Steefel, C.I., 2007. Geochemical kinetics and transport. In: Brantley, S., Kubicki, J., White, A. (Eds.), Kinetics of Water–Rock Interaction. Springer, New York, pp. 545–589.
Steuber, T., Korbar, T., Jelaska, V., Gušić, I., 2005. Strontium-isotope stratigraphy of Upper Cretaceous platform carbonates of the island of Brač (Adriatic Sea, Croatia): implications for global correlation of platform evolution and biostratigraphy. Cretac. Res. 26, 741–756.
Stirling, R.A., Davie, C.T., Glendinning, S., 2013. Numerical modelling of desiccation crack induced permeability. Proceedings of the 18th International Conference on Soil Mechanics and Geotechnical Engineering, Paris, pp. 813–816.
Stow, D.A., Faugeres, J.-C., Viana, A., Gonthier, E., 1998. Fossil contourites: a critical review. Sediment. Geol. 115, 3–31.
Tardy, Y., Nahon, D.B., 1985. Geochemistry of laterites. Stability of Al-goethite, Al-hematite and Fe3 kaolinite in bauxites and ferricretes. An approach to the mechanism of concretion formation. Am. J. Sci. 285, 865–903.
Taylor, S.R., McLennan, S.M., 1985. The Continental Crust: Its Composition and Evolution. Blackwell, Oxford.

Tiepolo, M., 2003. In situ Pb geochronology of zircon with laser ablation inductively coupled plasma-sector field mass spectrometry. Chem. Geol. 199, 159–177.
van Achterbergh, E., Ryan, C., Jackson, S., Griffin, W., 2001. Data reduction software for LAICPMS. In: Sylvester, P. (Ed.), Laser Ablation ICPMS in the Earth Science. Mineralogical Association Canada 29, pp. 239–243.
Vidal, O., Goffé, B., Arndt, N., 2013. Metals for a low-carbon society. Nat. Geosci. 6, 894–896.
Viers, J., Wasserburg, G.J., 2004. Behavior of Sm and Nd in a lateritic soil profile. Geochim. Cosmochim. Acta 68, 2043–2054.
Vrielynck, B., Dercourt, J., Cottereau, N., 1996. The Tethys: An Ocean Broken By Seuils Lithospheriques. In: Nairn, A.E.M., Ricou, L.-E., Vrielynck, B., Dercourt, J. (Eds.), The Tethys Ocean. Springer Science, New York, pp. 495–511.
Wang, Q., Deng, J., Liu, X., Zhang, Q., Sun, S., Jiang, C., Zhou, F., 2010. Discovery of the REE minerals and its geological significance in the Quyang bauxite deposit, West Guangxi, China. J. Asian Earth Sci. 39, 701–712.
Weaver, P.P.E., Wynn, R.B., Kenyon, N.H., Evans, J., 2000. Continental margin sedimentation, with special reference to the north-east Atlantic margin. Sedimentology 47, 239–256.
Wiedenbeck, M., Alle´, P., Corfu, F., Griffin, W.L., Meier, M., Oberli, F., von Quadt, A., Roddick, J.C., Spiegel, W., 1995. Three natural zircon standards for U–Th–Pb, Lu–Hf, trace element and REE analyses. Geostand. Newslett. 19, 1–23.
Wilkinson, M., Dampier, M.D., 1990. The rate of growth of sandstone-hosted calcite concretions. Geochim. Cosmochim. Acta 54, 3391–3399.
Yu, W., Ruihu, W., Qilian, Z., Yuansheng, D., Yue, C., Yuping, L., 2014. Mineralogical and geochemical evolution of the Fusui bauxite deposit in Guangxi, South China: from the original Permian orebody to a Quarternary Salento-type deposit. J. Geochem. Explor. 146, 75–88.
Yuste, A., Bauluz, B., Mayayo, M.J., 2014. Genesis and mineral transformations in Lower Cretaceous karst bauxites (NE Spain): climatic influence and superimposed processes. Geol. J. http://dx.doi.org/10.1002/gj.2604.
Zappaterra, E., 1994. Source-rock distribution model of the Periadriatic region. AAPG Bull. 78, 333.
Zarasvandi, A., Charchi, A., Carranza, E.J.M., Alizadeh, B., 2008. Karst bauxite deposits in the Zagros Mountain Belt, Iran. Ore Geol. Rev. 34, 521–532.
Zarcone, G., Petti, F.M., Cillari, A., Di Stefano, P., Guzzetta, D., Nicosia, U., 2010. A possible bridge between Adria and Africa: new palaeobiogeographic and stratigraphic constraints on the Mesozoic palaeogeography of the Central Mediterranean area.